J. Fluid Mech. (2026), *vol.* 1037, A62, doi:10.1017/jfm.2026.11715

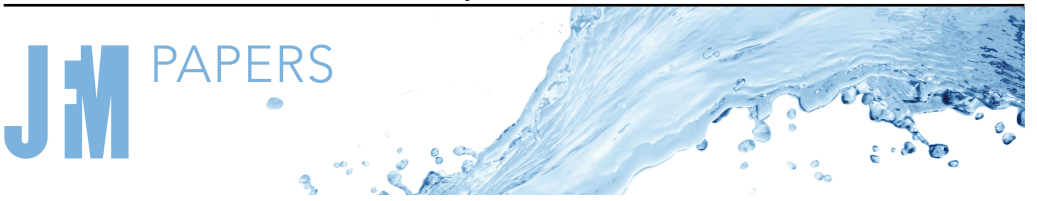

Multiscale dynamics of inertial particles in turbulence with and without the effect of gravitational settling

Thibault Maurel-Oujia[1,2], **Keigo Matsuda**[2] and **Kai Schneider**[1]

[1]Institut de Mathématiques de Marseille, CNRS, Aix-Marseille Université, Marseille, France

[2]Japan Agency for Marine-Earth Science and Technology (JAMSTEC), Yokohama, Japan

Corresponding author: Thibault Maurel-Oujia, tmaurelo@purdue.edu

(Received 7 May 2025 UTC; revised 27 December 2025 UTC; accepted 15 May 2026 UTC)

We investigate the dynamics of inertial heavy particles in three-dimensional homogeneous isotropic turbulence, both with and without gravitational settling, by means of direct numerical simulation over a range of Stokes numbers ($0.05 \leqslant St \leqslant 5$) and at a Taylor-microscale Reynolds number $Re_\lambda = 204$. Utilising a modified Voronoi tessellation, we compute the divergence, curl and helicity of particle velocities to quantify particle cloud self-organisation, including clustering, as well as vortical and swirling motions within particle clouds. We perform a novel graph-based multiresolution analysis by applying a wavelet decomposition to the divergence and curl of the particle velocities, and thus assess the clustering dynamics across multiple scales. Scales at which cluster formation and destruction are most active can hence be identified. In addition, we quantify and analyse the impact of the Stokes numbers and gravity on the divergence, rotational and swirling motions of particle clouds. As quantified in the wavelet energy spectra, gravitational settling is shown to affect the scale distribution of divergence and curl. We observe that the dominant particle dynamics is shifted toward larger scales while amplitude decrease for large Stokes numbers. In the absence of gravity the activity becomes increasingly concentrated at smaller scales for large Stokes numbers, consistent with the emergence of caustics. These gravitational effects become more pronounced at higher Stokes numbers, where particle motion transitions from relatively erratic without gravity to more coherent swirling patterns with gravity, as also reflected by the helicity of the particle velocity, which indicates an increased alignment and anti-alignment between the particle velocity and the particle vorticity.

Key words: isotropic turbulence, multiphase flow, particle/fluid flows

1. Introduction

Inertial heavy particles are ubiquitous in numerous industrial and environmental turbulent flows, such as in the dispersion of pollutants in the atmosphere, the formation of clouds, sediment transport in rivers or spray combustion. The dynamics of these particles plays a crucial role in shaping the characteristics and outcomes of such flows, making their study an important area of research. For reviews on the behaviour of inertial particles influenced by different parameters, such as their mass, volume fraction, density and the effects of gravitational acceleration, we refer the reader to Kuerten (2016) and Brandt & Coletti (2022). For a recent synthesis of clustering, caustics and gravitational effects in turbulent particle dynamics, including an overview of statistical models for the dynamics of heavy particles, we refer the reader to the review by Bec, Gustavsson & Mehlig (2024).

It is well known from both computational and experimental studies that inertial particles within turbulent flows exhibit non-uniform spatial distributions, known as inertial particle clustering, which lead to the formation of distinct void and cluster regions (Squires & Eaton 1990, 1991). The Stokes number, which quantifies how the dynamics of inertial particles deviates from that of fluid particles, is defined as the ratio between the particle's response time to changes in the flow and the characteristic time scale of the turbulence. Due to their inertia, heavy particles tend to be ejected from vortices by centrifugal effects and concentrate in regions of low vorticity and high strain rates. This mechanism is known as preferential concentration and is observed primarily in the case of small Stokes numbers $St \ll 1$, where the behaviour of particles is correlated with that of the underlying flow structure (Gustavsson & Mehlig 2011). For such small Stokes numbers, a relationship between the divergence of the inertial particle velocity and the background flow field was derived by Robinson (1956) and Maxey (1987). This relation indicates that regions with large negative values of the second invariant of the velocity-gradient tensor of the fluid, i.e. regions with high strain rate, are more conducive to the concentration of inertial particles for small Stokes numbers (Squires & Eaton 1990). Numerous theoretical analyses on inertial particle clustering have been conducted based on the preferential concentration mechanism (e.g. Elperin, Kleeorin & Rogachevskii 1996; Chun *et al.* 2005; Esmaily-Moghadam & Mani 2016). Gustavsson & Mehlig (2011) have shown that multiplicative amplification contributes substantially to clustering at $St = \mathcal{O}(1)$, whereby random contractions and expansions of particle clouds along their trajectories lead to a net volume contraction and thus to fractal clustering. Consistent with this, clusters and void regions continue to be observed for larger Stokes numbers of the order of $St = \mathcal{O}(1)$, even though the particle velocity depends much more on their path-history interactions with the turbulent flow (Bragg, Ireland & Collins 2015). For $St \geqslant \mathcal{O}(1)$, the velocity of the particles can be multivalued, i.e. particles located at the same position may possess different velocities. Such regions are referred to as caustics (Wilkinson & Mehlig 2005; Wilkinson, Mehlig & Bezuglyy 2006; Bec *et al.* 2010). To elucidate clustering of inertial particles for $St \geqslant \mathcal{O}(1)$, the concept known as the 'sweep-stick mechanism' has been proposed (Chen, Goto & Vassilicos 2006; Goto & Vassilicos 2006; Goto & Vassilicos 2008; Coleman & Vassilicos 2009). While earlier studies often described it as particles being swept by larger-scale flow motions and sticking to stagnation points of the fluid acceleration, more recent work by Oka & Goto (2021) highlights that, at high Reynolds numbers, clustering arises from the interaction with a hierarchy of coherent vortices and can be characterised using a coarse-grained acceleration field. As discussed in Meibohm *et al.* (2020) and Bec *et al.* (2024), the heavy particle dynamics is naturally described in the six-dimensional phase space of position and velocity. Because the dynamics is dissipative, phase-space volumes contract on average. Combined with turbulent stretching and folding,

this contraction drives trajectories onto a time-evolving fractal attractor whose multifractal geometry underlies the intermittency of particle separations and relative velocities. When projected onto configuration space, distinct velocity branches then overlap at the same location, so that the particle velocity becomes multivalued and caustics form.

Another important parameter that significantly impacts particle clustering is the effect of gravitational acceleration, which introduces particle-velocity anisotropy. The impact of gravity cannot always be neglected, as in cases where the gravitational settling speeds of particles are much larger than the Kolmogorov velocity, which leads to a substantially altered response of the particles to the underlying flow (Bec, Homann & Ray 2014; Gustavsson, Vajedi & Mehlig 2014; Ireland *et al.* 2016*b*). Bec *et al.* (2014) showed, using direct numerical simulation (DNS), that gravity can either reduce or enhance particle clustering depending on the Stokes number, thereby introducing significant anisotropy to their spatial distribution. Gustavsson *et al.* (2014) showed that gravitational settling shortens the time that particles remain within the same turbulent eddies, thereby weakening centrifuge-type preferential sampling for $St \lesssim 1$. When particles settle sufficiently fast, they see the fluid-velocity gradients as an effectively white-noise signal along their paths, which alters the clustering mechanisms and enables substantial clustering by multiplicative amplification. For a comprehensive DNS study with gravity, including evaluations of the strain rate and rotation rate tensors at inertial particle positions and analyses of inertial particle kinetic energy, acceleration and relative velocities to quantify the influence of turbulent flow structures on inertial particle dynamics, we refer the reader to Ireland *et al.* (2016*b*). In contrast, for higher Stokes numbers, gravity can actually enhance clustering by modulating the ratio of drift to diffusion, causing particles to settle through the flow in a manner that accentuates their distribution patterns at certain scales, thereby reinforcing non-uniform spatial arrangements. It has also been reported that this gravitational influence introduces notable anisotropy in velocity-gradient statistics and particle accelerations, reflecting the fact that particles experience different flow regions more rapidly in the vertical direction than in the horizontal directions.

Clustering has also been investigated in Matsuda *et al.* (2014, 2017) using the energy spectrum, computed using the Fourier transform of particle number-density fluctuation for turbulent clustering droplets with and without the gravitational effects for several Stokes numbers. These spectral analyses quantify clustering as a function of wavenumber and identify the dominant scales and their dependence on St. They also characterise how gravitational settling redistributes spectral energy across scales. In order to obtain high-order scale-dependent statistics such as skewness and flatness, a similar method based on the wavelet transform was developed in Matsuda, Schneider & Yoshimatsu (2021) to study particle clustering using the wavelet energy spectrum of particle number-density fluctuation. For a detailed analysis of the particle spectrum, we refer the reader to Saito & Gotoh (2018), who examine the time evolution of number-density spectra for cloud droplets in turbulence. However, these approaches have only been used from a static perspective (i.e. instantaneous descriptions from particle number density) and not from a dynamic one (i.e. the time evolution of particle number-density structures). A study of the scale-dependent particle dynamics could offer deeper insights into how particles behave across different scales of motion in turbulent flows. In many previous studies, most attention has been placed on preferential concentration mechanisms or on static distributions of particles, while their dynamic and multi-scale behaviour appears comparatively less explored.

Voronoi tessellation was used in Monchaux *et al.* (2010, 2012) to identify cluster and void regions in their studies of inertial particle clustering for different Stokes numbers.

Baker *et al.* (2017) use Voronoi volumes to study particle clustering and find that the clusters tend to align with the local vorticity vector, i.e. the clusters' primary axes (obtained from a singular value decomposition of the particle positions) are statistically aligned with the local vorticity direction. Although numerous works employing Voronoi-based methods have successfully characterised the instantaneous spatial arrangement of clusters and voids, they do not explicitly address the particle dynamics. Additionally, the influence of multiple length scales on the development of these clusters is less explored in such analyses. In our previous work, we developed tessellation-based techniques that quantify the divergence, curl and helicity of the particle velocity by analysing the temporal evolution of the tessellation cells (Oujia, Matsuda & Schneider 2020; Maurel–Oujia *et al.* 2024). In this study, we focus on analysing particle clouds, i.e. localised groups that move together. To go beyond static observations, we utilise the tessellation-based technique to quantify the dynamics of particle clouds and propose the application of multiresolution analysis techniques (Matsuda *et al.* 2022) to analyse the scale-dependent dynamics of particle motion. This framework allows us to investigate how particles behave and form structures across different scales within the flow.

In this study, we aim to clarify the dynamics of one-way coupled inertial particles through high-resolution DNS of homogeneous isotropic turbulence (HIT), considering different Stokes numbers and assessing the influence of gravity. Previous DNS studies have documented how gravity modifies clustering intensity, anisotropy and relative velocities of inertial particles (Bec *et al.* 2014; Ireland *et al.* 2016*b*), however, it remains unclear how these mechanisms manifest for the different scales of motion. To this end, we propose to use the scale-dependent divergence, curl and helicity of the particle-velocity field, to quantify how inertia and gravity influence these quantities across scales and impact the particle dynamics. Specifically, our simulations focus on air flows containing water droplets that are sparsely distributed. This set-up is designed to replicate conditions representative of small-scale turbulence in atmospheric clouds. We adopt one-way coupling, whereby the carrier flow is prescribed and unaffected by the particles, and particle–particle collisions are neglected. In this setting, each particle can be regarded as an independent realisation sampling the same turbulent field, which enables robust ensemble statistics, following Matsuda *et al.* (2021). With the help of tools such as differential operators based on the volume change (Maurel–Oujia *et al.* 2024) and multiresolution analysis (Matsuda *et al.* 2022), we aim to improve our understanding of the dynamics of one-way coupled inertial particles, and to identify the impact of the particle inertia and the gravity on their behaviour. This is achieved by assigning to each particle a cell representing a portion of space, and by tracking the temporal evolution of each cell's volume to infer the local divergence and curl. By progressively merging adjacent cells and comparing the divergence and curl before and after each merging step, we evaluate these quantities across different spatial scales. This approach facilitates the identification of the length scales at which particle clustering is most active, provides the dynamics of quantities evaluated at different scales to characterise particle motion and offers insights into the coherence of particle motion relative to the various parameters taken into account.

The outline of the manuscript is as follows. In § 2, we provide a concise overview of the DNS that forms the basis of our analysis. The mathematical framework, the methods for computing differential operators of the particle velocity and the multiresolution technique are explained in § 3. In § 4, we apply the methods to inertial particle-laden flows, analysing flows without and with the influence of gravity. We study the effects of the Stokes number and gravity on the particle distribution, as well as on the divergence, curl and helicity of the particle velocity. Finally, conclusions are drawn in § 5.

2. Direct numerical simulation

2.1. *Fluid motion*

The fluid flow is governed by the incompressible three-dimensional Navier–Stokes equations, which are solved in a cubic domain with periodic boundary conditions, and are given by

$$\frac{\partial \boldsymbol{u}}{\partial t} + (\boldsymbol{u}\cdot\nabla)\boldsymbol{u} = -\frac{1}{\rho}\nabla p + \nu\nabla^2\boldsymbol{u} + \boldsymbol{F}, \tag{2.1}$$

$$\nabla\cdot\boldsymbol{u} = 0, \tag{2.2}$$

where $\boldsymbol{u}$ represents the fluid velocity, p is the pressure, ρ is the fluid density, ν is the kinematic viscosity and $\boldsymbol{F}$ is the external force. A fourth-order central difference scheme is used for the advection and diffusion terms, while the second-order Runge–Kutta scheme is utilised for time integration. The velocity and pressure are coupled by the highly simplified marker and cell method (Hirt & Cook 1972). Statistically steady turbulence is achieved by applying an external force $\boldsymbol{F}$ using the reduced-communication forcing method (Onishi, Baba & Takahashi 2011). This approach sustains the intensity of large-scale eddies while ensuring high efficiency in parallel computing environments.

High-resolution DNS are performed in a three-dimensional periodic cubic computational domain with a side length of $2\pi L_0$ with $N_g^3 = 512^3$ grid points, where $L_0 = 0.0682$ m, and the characteristic velocity scale $U_0 = 0.2\,\mathrm{m\,s^{-1}}$. The kinematic viscosity is $\nu = 1.5\times10^{-5}\,\mathrm{m^2\,s^{-1}}$, corresponding to air. The root mean square of the velocity fluctuation, the energy dissipation rate and the Taylor-microscale Reynolds number of the obtained turbulence are characterised by $u_{rms}/U_0 = 1.01$, $\epsilon = 0.0395\,\mathrm{m^2\,s^{-3}}$, $Re_\lambda = \lambda u_{rms}/\nu = 204$, where λ is the Taylor microscale. Statistically steady turbulence was obtained by forcing at large scales. The DNS conditions for this simulation are the same as those in Matsuda, Onishi & Takahashi (2017).

2.2. *Particle motion*

Maxey's model for inertial heavy point particles with Stokes drag is used, i.e. the flow around particles is considered laminar. The particle motion is governed by

$$d_t\boldsymbol{x}_p = \boldsymbol{v}_p, \tag{2.3}$$

$$d_t\boldsymbol{v}_p = -\frac{\boldsymbol{v}_p - \boldsymbol{u}_p}{\tau_p} + \boldsymbol{f}_g. \tag{2.4}$$

Here, $\boldsymbol{u}_p$ is the fluid velocity interpolated at the particle location $\boldsymbol{x}_p$, $\boldsymbol{v}_p$ is the particle velocity, τ_p is the particle relaxation time defined as

$$\tau_p = \frac{\rho_p}{\rho_a}\frac{d_p^2}{18\nu}, \tag{2.5}$$

where d_p is the particle diameter, and $\boldsymbol{f}_g$ is an external force to the flow. The ratio between the particle density of water droplets ρ_p and the air density ρ_a is $\rho_p/\rho_a = 840$. In the scenario without gravity, the external force $\boldsymbol{f}_g$ is zero, and in the case with gravity, we have $\boldsymbol{f}_g = \boldsymbol{g} = (-g, 0, 0)^T$, where $g = 9.8\,\mathrm{m\,s^{-2}}$ and where the superscript ^{T} is the transposition operator. The Stokes number which characterises particle inertia is defined as $St = \tau_p/\tau_\eta$, where $\tau_\eta = (\nu/\epsilon)^{1/2}$ is the Kolmogorov time. Several non-dimensional parameters, given in table 1, represent the gravitational effect, such as the Froude number $Fr = \epsilon^{3/4}/(\nu^{1/4}g)$ and the non-dimensional terminal velocities $S_v = St/Fr$ (Woittiez, Jonker & Portela 2009; Bec *et al.* 2014). In this study, Fr is kept constant, and S_v therefore

St	0.05	0.1	0.2	0.5	1	2	5
S_v	0.34	0.68	1.36	3.39	6.79	13.6	33.9

Table 1. Physical parameters of the DNS computations with and without gravity: St denotes the Stokes number and S_v the non-dimensional terminal velocities in the gravitational case with constant Froude number ($Fr = 0.145$).

varies linearly with St. We thus refer to variations in St and S_v interchangeably, without further distinction. For the case of atmospheric flows where $\nu = 1.5 \times 10^{-5}\,\mathrm{m^2\,s^{-1}}$ and $g = 9.8\,\mathrm{m\,s^{-2}}$, the dimensional value of the energy dissipation rate ϵ in the present parameter setting is $395\,\mathrm{cm^2\,s^{-3}}$, which can be observed in cumulus and cumulonimbus clouds and close to strong cumulus clouds (Pinsky, Khain & Krugliak 2008). The present Stokes number range corresponds to particle radii from 8.85 to 88.5 μm, covering typical cloud droplets ($\sim 10\,\mu$m) and those in transition to drizzle droplets.

The number of particles N_p is 1.07×10^9 and simulations for seven distinct Stokes numbers are conducted, as detailed in table 1. For the different Stokes numbers, the particles are traced in the same flow. The parameters are similar to one of the datasets from Matsuda *et al.* (2017). Modulation of turbulence and collisions between droplets are neglected, as cloud droplets are typically diluted. Particles are one-way coupled, i.e. particles are influenced by the flow, but their impacts on the flow dynamics and interactions between particles are not considered. Given this set-up, the large number of particles does not affect the flow, and each particle can be seen as an individual manifestation of the possible positions and velocities within the turbulent flow under study (Matsuda *et al.* 2021). For reference, the ratios of the particle size to the Kolmogorov length are $a_p/\eta = 0.073$ for $St = 1$ and $a_p/\eta = 0.16$ for $St = 5$, where $a_p = d_p/2$ is the particle radius. The corresponding shear Reynolds numbers $(a_p/\eta)^2$ (Bec *et al.* 2024) are 5.4×10^{-3} and 2.7×10^{-2} for $St = 1$ and 5, respectively. These values are much smaller than unity, which supports the point-particle assumption. When the slip velocity of particles compared with that of the fluid is high, the particle Reynolds number is large, and thus the effects of nonlinear drag cannot be ignored. Gravity induces a high terminal velocity, leading to a significant relative velocity. Consequently, for a Stokes number of 1, the particle Reynolds number is unity. As in Baker *et al.* (2017), we choose not to correct for the nonlinear drag in order to focus on the fundamental point-particle kinematics. Particles are initially randomly distributed and are injected into the fully developed turbulent flow at time $t = 10T_0$, where $T_0 = L_0/U_0$. Five snapshots are saved during the time range $21T_0 \leqslant t \leqslant 25T_0$.

3. Analysis methods

In this section, we present the core mathematical tools employed in our study to analyse the particle-velocity divergence, curl and helicity in turbulent flows. The objective is to provide a clear and comprehensive understanding of the methodologies that underpin our analysis. Our discussion will encompass an exploration of tessellations, which are essential for assigning a cell to each particle. We will also present the computation of divergence, focusing on how changes in volume can reveal intricate details about particle behaviour. The quantities considered are finite-time observables sampled along particle trajectories, and the divergence is interpreted in a distributional sense from finite-time changes of the cell volume. For inertial particles, the underlying dynamics lives in the six-dimensional

phase space ($\boldsymbol{x}$, $\boldsymbol{v}$). Upon projection to configuration space, however, the particle velocity can become multivalued and may not be continuous in caustic regions. From an Eulerian point of view, one can introduce a phase-space description based on the Boltzmann equation, and the configuration space fields ($\boldsymbol{x}$-space), such as the particle number density and the mean particle velocity, are then obtained by the ensemble average of possible particle velocities at each position, which yields single-valued continuum fields (Kasbaoui, Koch & Desjardins 2019). Nevertheless, in our analyses, a piecewise constant velocity field is introduced for each tessellation cell and the effective particle-velocity divergence can be computed as it is defined from finite-time changes of tessellated cell volumes. By definition, the divergence values computed in caustic regions should be different from the divergence of the single-valued ensemble-averaged velocity due to the multi-valued nature. In caustic regions, the divergence values become intermittent, and we can consider that such intermittent divergence values are an indicator of caustic regions. Additionally, the application of multiresolution techniques, using hierarchical cell coarsening, where smaller cells are embedded into larger ones, is explored to capture the dynamic interplay of particles across various scales. By construction, increasing the analysis scale smooths trajectories and reduces the influence of caustics. This multiresolution approach recovers the particle behaviour at each scale as actually sampled by the particles, from the finest inter-particle separations up to larger scales that characterise interactions between clusters. This approach is designed to offer a thorough and nuanced perspective on the particle dynamics within turbulent flows.

3.1. *Modified Voronoi tessellations*

Voronoi tessellation (Voronoi 1908), a fundamental tool in spatial analysis, partitions the space seeded with particles into distinct cells based on proximity. Each cell in a Voronoi diagram, denoted as $\mathscr{C}_{p_i}$, encloses a region of space closer to its generating particle p_i than to any other particle, representing the influence domain of that particle. This tessellation is advantageous as it does not introduce an arbitrary length scale and is reflective of the local particle density. The Voronoi cell volumes are inversely related to the particle density, offering a means to identify clusters and voids in the particle distribution. A further refinement, the modified Voronoi tessellation, utilises the centre of gravity of the Delaunay cell (the dual graph of the Voronoi tessellation) to define the vertices of the cell. This modification, as proposed in Maurel–Oujia *et al.* (2024), enhances the stability and accuracy in computing differential operators. This tessellation is called modified Voronoi tessellation. To construct the Delaunay tessellation, we utilise the Computational Geometry Algorithms Library (CGAL) (Fabri & Pion 2009), a versatile C++ library renowned for its efficiency in handling complex geometric computations. The implementation of CGAL is advantageous due to its computational complexity of $\mathcal{O}(N \log(N))$, where N represents the number of particles. Furthermore, CGAL's capabilities extend to parallel computing, allowing for more efficient processing and analysis of large-scale particle datasets in our turbulent flow studies.

3.2. *Differential operators computation via volume change*

The cornerstone of the approach, introduced in Oujia *et al.* (2020) and developed in Maurel–Oujia *et al.* (2024), lies in the application of the conservation equation for particle number density n, expressed as

$$D_t n = \partial_t n + \boldsymbol{v} \cdot \boldsymbol{\nabla} n = -n \boldsymbol{\nabla} \cdot \boldsymbol{v}, \tag{3.1}$$

where $D_t n$ denotes the Lagrangian derivative of n, and $\boldsymbol{v}$ is the particle velocity.

The local number density n_p averaged over a modified Voronoi cell is defined as the inverse of the cell's volume V_p, i.e. $n_p = V_p^{-1}$. By considering the particle density at two subsequent time instants t^k and $t^{k+1} = t^k + \Delta t$, where Δt is the time step, and substituting n by this discrete approximation n_p, the finite-time discrete divergence of particle velocity can be defined as

$$\mathcal{D}(\boldsymbol{v}_p) = -\frac{1}{n_p} D_t n_p = \frac{2}{\Delta t} \frac{V_p^{k+1} - V_p^k}{V_p^{k+1} + V_p^k}, \tag{3.2}$$

where $\boldsymbol{v}_p$ is the particle velocity $\boldsymbol{v}$ evaluated at the particle's position $\boldsymbol{x}_p$, and $\mathcal{D}(\boldsymbol{v}_p)$ is bounded, i.e. it satisfies $|\mathcal{D}(\boldsymbol{v}_p)| \leqslant 2/\Delta t$ by construction (Oujia *et al.* 2020; Apte *et al.* 2022). The identity above is understood in the sense of distributions, with the particle velocity $\boldsymbol{v}_p$ treated in the distributional framework and therefore admitting derivatives of arbitrary order (Schwartz 1950). Accordingly, $\mathcal{D}$ denotes the action of the distributional divergence on a test function related to the characteristic function of the cell, and can be understood mathematically as a weak formulation of the divergence operator over that cell.

Note that the discrete divergence can be rewritten in logarithmic form (Maurel–Oujia *et al.* 2024)

$$\mathcal{D}(\boldsymbol{v}_p) = \frac{1}{\Delta t} \ln\left(\frac{V_p^{k+1}}{V_p^k}\right) + \mathcal{O}(1/N_p). \tag{3.3}$$

Using the definition of the asymptotic growth rate of the volume $V_6(t)$ of a six-dimensional phase-space region (Bec *et al.* 2024)

$$\sigma_6 = \lim_{t\to\infty} \frac{1}{t} \ln\left(\frac{V_6(t)}{V_6(0)}\right) = \sum_{i=1}^{6} \lambda_i, \tag{3.4}$$

where λ_i are the Lyapunov exponents ordered as $\lambda_1 \geqslant \cdots \geqslant \lambda_6$, we can deduce that the discrete divergence, which is different, is a single-step configuration-space analogue of a volume growth rate. The growth rate σ_6 quantifies the long-time contraction rate of phase-space volumes and characterises the dissipative nature of the particle dynamics.

Similarly to the divergence, the curl of the particle velocity, which represents the circulation of the velocity field of particles over a cell $\mathscr{C}_p$, can be computed using the method based on the volume change (Maurel–Oujia *et al.* 2024). The discrete curl of the particle velocity $\boldsymbol{\mathcal{C}}(\boldsymbol{v}_p)$ is obtained by

$$\boldsymbol{\mathcal{C}}(\boldsymbol{v}_p) = \begin{pmatrix} \mathcal{C}_x(\boldsymbol{v}_p) \\ \mathcal{C}_y(\boldsymbol{v}_p) \\ \mathcal{C}_z(\boldsymbol{v}_p) \end{pmatrix} = \begin{pmatrix} \mathcal{D}\left(-\boldsymbol{v}_{p,x}^{\perp}\right) \\ \mathcal{D}\left(-\boldsymbol{v}_{p,y}^{\perp}\right) \\ \mathcal{D}\left(-\boldsymbol{v}_{p,z}^{\perp}\right) \end{pmatrix}, \tag{3.5}$$

where $\boldsymbol{v}_{p,x}^{\perp} = \boldsymbol{L}_x \boldsymbol{v}_p$, $\boldsymbol{v}_{p,y}^{\perp} = \boldsymbol{L}_y \boldsymbol{v}_p$ and $\boldsymbol{v}_{p,z}^{\perp} = \boldsymbol{L}_z \boldsymbol{v}_p$. Here, $\boldsymbol{L}_x$, $\boldsymbol{L}_y$ and $\boldsymbol{L}_z$ are the rotation matrices around the x, y and z-axes, respectively, which are defined as

$$\boldsymbol{L}_x = \begin{pmatrix} 0 & 0 & 0 \\ 0 & 0 & -1 \\ 0 & 1 & 0 \end{pmatrix}, \boldsymbol{L}_y = \begin{pmatrix} 0 & 0 & 1 \\ 0 & 0 & 0 \\ -1 & 0 & 0 \end{pmatrix} \text{ and } \boldsymbol{L}_z = \begin{pmatrix} 0 & -1 & 0 \\ 1 & 0 & 0 \\ 0 & 0 & 0 \end{pmatrix}. \tag{3.6}$$

For additional details on the method and its validation, we refer the reader to Maurel–Oujia *et al.* (2024).

A relevant quantity related to the curl of particle velocity is the helicity. Helicity is defined as the scalar product of vorticity and velocity, and provides insight into the geometrical alignment of these vectors, allowing us to quantify the swirling motion of particle clouds. The relative helicity of the particle velocity is defined as

$$\mathcal{H}(\boldsymbol{v}_p) = \frac{\boldsymbol{v}_p \cdot \boldsymbol{\mathcal{C}}(\boldsymbol{v}_p)}{||\boldsymbol{v}_p||_2 \, ||\boldsymbol{\mathcal{C}}(\boldsymbol{v}_p)||_2}, \tag{3.7}$$

and yields the cosine of the angle between the two vectors at each particle position. The values of helicity span from -1 to $+1$, where -1 indicates a complete anti-alignment and $+1$ signifies a perfect alignment between the vorticity and velocity, both indicative of pronounced swirling motion. A helicity value of 0 corresponds to a two-dimensional motion, denoting an orthogonal relationship between vorticity and velocity.

3.3. *Multiresolution technique*

In this study, we utilise the multiresolution analysis method developed by Matsuda *et al.* (2022). This method allows us to examine the dynamics of the system across multiple scales and to extract meaningful information about particle distributions and associated quantities such as divergence and curl.

Our multiresolution analysis is constructed upon Delaunay tessellation graphs that represent neighbouring particle cells in physical space. These graphs are organised across multiple levels $l = 0, \ldots, L-1$, where the level index l increases as the scale becomes coarser.

For graph coarsening, we adopt the half-edge collapse operator as outlined by Kobbelt *et al.* (1998). This operator merges one vertex with an adjacent vertex, selecting pairs based on the minimum volume attribute of their associated tessellation cells. The coarsening algorithm involves marking and merging vertices and updating volume values to ensure volume conservation. Specifically, the updated volume for a vertex at level $l+1$ is given by $V_i^{l+1} = V_{2i}^l + V_{2i+1}^l$.

Regarding the wavelet transform on these graphs, we consider a signal $s_i^0 = s^0(x_{p,i})$ defined at discrete particle positions. The transform is based on the conservation equation $V_i^{l+1}\overline{s}_i^{l+1} = V_{2i}^l \overline{s}_{2i}^l + V_{2i+1}^l \overline{s}_{2i+1}^l$, where $\overline{s}_i^l$ represents the signal at the ith vertex on the graph at level l. The projection operator is defined as

$$\overline{s}_i^{l+1} = \frac{1}{V_i^{l+1}} \left(V_{2i}^l \overline{s}_{2i}^l + V_{2i+1}^l \overline{s}_{2i+1}^l \right). \tag{3.8}$$

For the prediction operator, we assume that the predicted signals at the finer level are equal to the projected signals at the coarser level, i.e. $\overline{s}_i^{l+1}$. Consequently, the detail coefficients are calculated as the difference between the original and predicted signals using

$$d_i^{l+1} = \frac{V_{2i}^l}{V_i^{l+1}} \left(\overline{s}_{2i+1}^l - \overline{s}_{2i}^l \right). \tag{3.9}$$

The detail coefficients represent the local fluctuation of the field between two adjacent merged cells. The wavelet energy spectrum is defined as

$$\mathcal{E}_s(k_V) = \frac{N_l M_2 \left[\sigma_i^l d_i^l \right]}{(2\pi)^D \Delta k_V}, \tag{3.10}$$

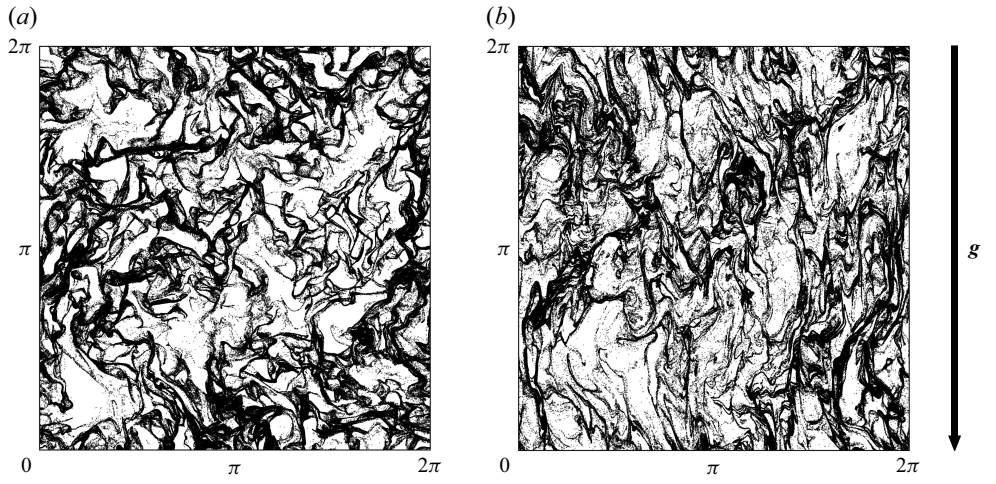

Figure 1. Two-dimensional slices of thickness $2\pi/1024$ in the yx-plane of the inertial particle positions (a) without and (b) with gravity for $St = 2$.

where Δk_V is the bandwidth of the wavelets at each level l and $\sigma_i^{l+1} = \sqrt{V_i^{l+1} V_{2i+1}^l / V_{2i}^l}$ is the scaling factor required to achieve L^2 normalisation. The volume-based wavenumber k_V is defined as

$$k_V = \pi \left(\frac{1}{N_l} \sum_{i=1}^{N_l} V_i^l \right)^{-1/3}, \tag{3.11}$$

where N_l is the total number of detail coefficients at level l. The term $M_2[d_i^l]$ is the second-order moment of the detail coefficients, computed as $M_2[d_i^l] = (1/N_l) \sum_{i=1}^{N_l} (d_i^l)^2$. For more details on multiresolution analysis of tessellations we refer the reader to Matsuda *et al.* (2022) and Matsuda, Maurel-Oujia & Schneider (2026).

4. Results and discussions

Figure 1 shows the spatial distribution of particles in two-dimensional slices of the domain for $St = 2$ without and with gravity. The particle distribution is represented in the yx-plane, with y as the abscissa and x as the ordinate since gravity points in the negative x direction. This orientation is chosen to make the interpretation of the figures more intuitive for the reader, and the same is done for the other spatial visualisations throughout this paper. In figure 1, we can observe non-uniform particle distributions characterised by pronounced clusters and voids, i.e. clustering. It is well known that the particle distribution depends on the Stokes number (Squires & Eaton 1990, 1991). Figure 1 also demonstrates that gravity impacts the particle distribution. In the present case, for instance, we can observe an elongation of clusters in the vertical direction, i.e. the direction of gravity. In the following, we will therefore seek to quantify the impact of the Stokes number and gravity on the behaviour of inertial particles.

In this section, we present the various results obtained for the volume, divergence, curl and helicity of inertial particles, for both cases without and with the influence of gravity. Several observations are consistent with results reported in previous studies (Bec *et al.* 2014; Gustavsson *et al.* 2014; Ireland *et al.* 2016*a*,*b*). We include them directly in the

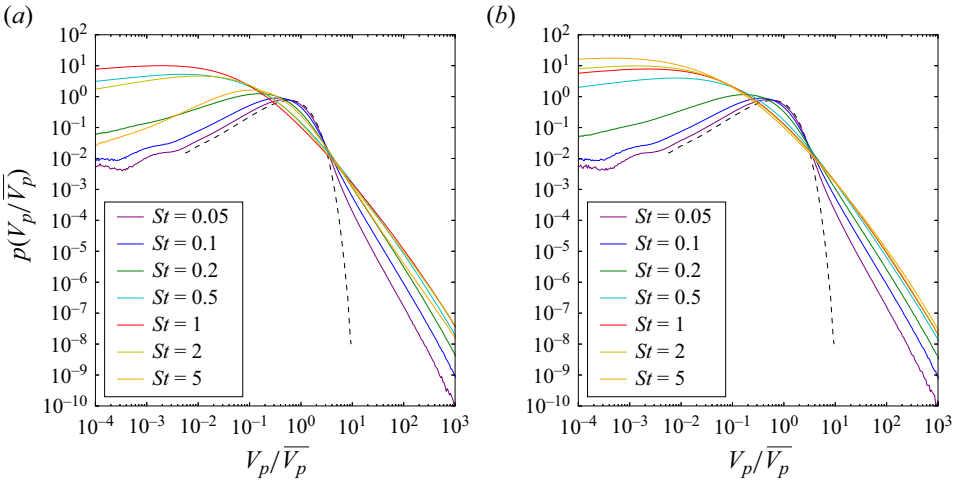

Figure 2. The PDFs of volume of modified Voronoi tessellation normalised by the mean $V_p/\overline{V_p}$ for different Stokes numbers (*a*) without and (*b*) with gravity. The black dashed line represents the volume distribution in the case of the same number of randomly distributed particles.

following subsections to provide a consistent baseline and to organise the subsequent interpretation of the new results. The presented statistics, including the probability distribution functions (PDFs), variance and flatness, are obtained by averaging over five snapshots, in which we have 1.07×10^9 particles per snapshot. The wavelet energy spectrum is computed from one snapshot with 1.34×10^8 particles due to limitations of the computational resources.

As shown in Appendix A, reducing the number of particles alters neither the shape nor the amplitude of the spectral distribution of energy although this reduction shifts the distribution slightly towards larger scales. Despite this scale shift, we anticipate that changing the number of particles does not affect comparisons involving the Stokes number, indicating that the key conclusions remain consistent.

4.1. *Volume distribution of inertial particle cells*

To examine the effects of particle inertia and external forces, such as gravity, on how particles are clustered, we explore the volume distribution of modified Voronoi tessellations. Figure 2 shows the PDFs of the volume of modified Voronoi tessellations normalised by the mean $V_p/\overline{V_p}$ for different Stokes numbers, both (a) without and (b) with gravity. These visualisations provide insights into the spatial distribution and clustering behaviour of inertial particles. Similarly to Monchaux, Bourgoin & Cartellier (2010), we define cluster cells as cells that have a volume smaller than the left intersection value ($V_p/\overline{V_p} \approx 0.4$) of the PDF of the volume of inertial particles and the PDF of the volume of randomly distributed particles, and void cells as the cells that have a volume larger than the right intersection value ($V_p/\overline{V_p} \approx 3$). In the gravity-free case, it can be observed that, as the Stokes number increases and gets closer to 1, the number of cluster cells increases, and then decreases after exceeding $St = 1$. This has also been observed in Dejoan & Monchaux (2013) and Baker *et al.* (2017), although here we show the volume of modified Voronoi cells and not that of the classical Voronoi. For void cells, a similar behaviour is observed, i.e. the number of void cells increases up to $St = 1$, and then slightly decreases. This illustrates that the clustering is the most pronounced for $St \approx 1$. In the case with gravity, the increasing trend in the number of cluster cells continues even for $St \geqslant 1$, in contrast to

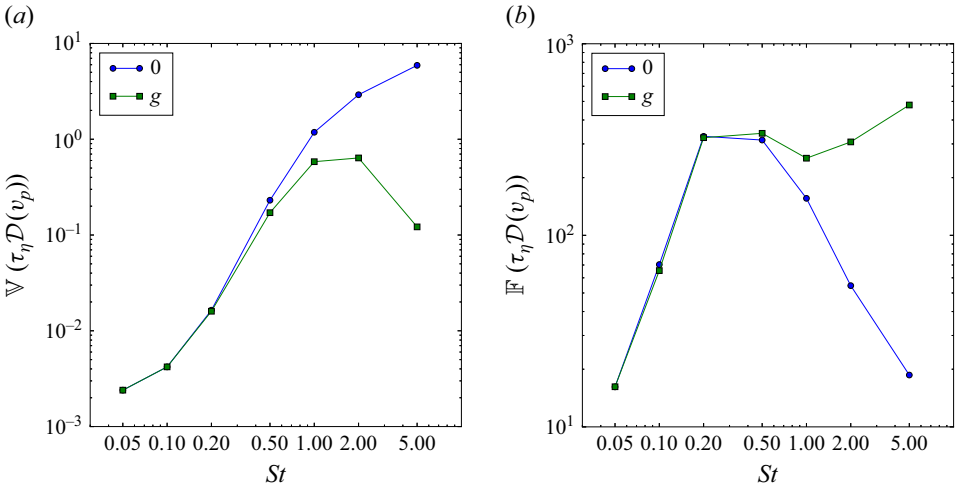

Figure 3. (*a*) Variance $\mathbb{V}$ and (*b*) flatness $\mathbb{F}$ of the particle-velocity divergence $\mathcal{D}(\boldsymbol{v}_p)$ normalised by the Kolmogorov time scale τ_η for different Stokes numbers without ($\boldsymbol{f}_g = \boldsymbol{0}$) and with ($\boldsymbol{f}_g = \boldsymbol{g}$) gravity.

the gravity-free case. Similarly, for void cells, their number continues to increase slightly. Thus, the clustering is more pronounced persistently as the Stokes number increases even for Stokes numbers higher than 1.

4.2. *Divergence of particle velocity*

In this subsection, we aim to understand how inertia and gravitational forces affect particle-velocity divergence, using tessellation-based divergence derived from modified Voronoi cell volume changes, as detailed in § 3.2. This understanding is crucial as the clustering formation and destruction of particles is inherently related to the particle-velocity divergence. By examining the particle-velocity divergence across different Stokes numbers, we assess the influence of gravity and inertia on particle motion in turbulent flows, providing insights into their dynamic behaviour.

Figure 3 shows the variance and flatness of the particle-velocity divergence for different Stokes numbers with and without gravity. Here, the variance is defined as $\mathbb{V}(X) = \langle (X - \langle X \rangle)^2 \rangle$, and the flatness by $\mathbb{F}(X) = \langle (X - \langle X \rangle)^4 \rangle / \langle (X - \langle X \rangle)^2 \rangle^2$, where $\langle \cdot \rangle$ denotes the ensemble average. Variance offers insight into the average level of divergence fluctuation, while flatness, a normalised fourth-order statistical moment, provides an indication of the distribution's tails. Specifically, high flatness values signify the presence of more statistically extreme events, characteristic of non-Gaussian and spatially intermittent behaviour. For a Gaussian distribution, the flatness value is equal to 3. For the corresponding PDFs see Appendix B.

For the case without gravity, we observe that the variance increases with the Stokes number. This is consistent with the expectation that particles exhibit a greater tendency to converge or to diverge due to the large particle relaxation time. The flatness also increases with the Stokes number for $St \leqslant 0.2$, but then decreases with the Stokes number for $St \geqslant 0.2$. This could suggest that the particle-velocity divergence is less intermittent for $St \leqslant \mathcal{O}(1)$.

We observe that the statistics for the particle-velocity divergence are similar in both scenarios without and with gravity for $St \leqslant 0.2$, i.e. $S_v \leqslant 1.36$. For $St \geqslant 0.5$ (i.e. $S_v \geqslant 3.39$), we can observe a discrepancy in both variance and flatness between the two cases for the

absence and presence of gravity. These observations are expected, as notable changes are typically anticipated when $S_v \geqslant \mathcal{O}(1)$ (refer to table 1).

In the scenario with gravity for $St \geqslant 0.5$ (i.e. $S_v \geqslant 3.39$), the variance is smaller than that in the scenario without gravity. It increases along with St up to $St = 2$ (i.e. $S_v = 13.6$), although at a smaller rate compared with the gravity-free case, and decreases for $St > 2$. The flatness, on the other hand, shows a decrease from $St = 0.5$ to $St = 1$ although it increases with St for $St \geqslant 1$. The increase in the flatness for $St \geqslant 1$ with gravity, suggests a transition to a different regime due to strong gravitational effects.

In Ireland *et al.* (2016*b*), the variance of relative particle velocities, both parallel and perpendicular to the separation vector, is examined. It is shown that gravity reduces the variance of relative velocities at small separations, with a more significant reduction as the Stokes number increases. This reduction in the relative velocities is explained by the fact that gravity reduces the effect of the path-history interactions (Gustavsson *et al.* 2014; Ireland *et al.* 2016*b*). This effect could also explain the observed reduction in the variance of the particle-velocity divergence in the presence of gravity, compared with the case without gravity.

Figure 4 shows the spatial distribution of particles in two-dimensional slices of thickness $2\pi/1024$, i.e. half of the grid spacing, of the domain. The particle positions are represented by colours that correspond to the particle-velocity divergence $\mathcal{D}(\boldsymbol{v}_p)$. This visualisation is presented for three distinct Stokes numbers, both without and with gravity.

For the Stokes number of 0.1, as depicted in panels (*a*) and (*b*), we can see small void regions and a majority of the domain exhibits a nearly uniform distribution in cases both without and with gravity. The impact of gravity on the divergence values at the particle position appears significantly small. This observation is consistent with observations in the PDF of the divergence in figure 14.

For the Stokes number of 1, shown in panels (*c*) and (*d*), there is noticeable particle clustering. Here, we observe fine clusters and distinct void regions. Moreover, differences between the scenarios without and with gravity are apparent. In the absence of gravity, the distribution of clusters is isotropic, and we can see different types of clusters: clusters where all particles strictly converge or diverge, and clusters where some particles converge and others diverge within the same cluster. In contrast, with gravity, particles tend to align somewhat more with the direction of gravity, and clusters often exhibit more uniform divergence signs, i.e. clusters primarily composed of either converging or diverging particles.

At an even higher Stokes number of 5, as illustrated in panels (*e*) and (*f*), the influence of gravity is significant. In the absence of gravity, clusters are more dispersed, and void regions are less distinct compared with $St = 1$. Moreover, in the absence of gravity, at a given position, neighbouring particles can take significantly different divergence values, which is a local signature of caustics where the particle velocity becomes multivalued. These large positive and negative divergence values and the more diffuse clusters (i.e. less filamentary structures with reduced void contrast) observed at large Stokes numbers are consistent with model studies showing that caustics can weaken spatial fractal clustering in the sense that the spatial correlation dimension increases, potentially up to three (the dimension of physical space), as caustics become more prevalent (Meibohm *et al.* 2020). In contrast, gravity introduces noticeable anisotropy by significantly elongating clusters in the direction of gravity, similar to the observations reported in Ireland *et al.* (2016*b*). The divergence varies continuously within the domain, even though some locations of extreme variation can be observed. In this regime, there is a noticeable reduction in overall particle divergence compared with scenarios without gravity. This indicates that gravitational forces significantly influence particle trajectories. This could potentially reduce the

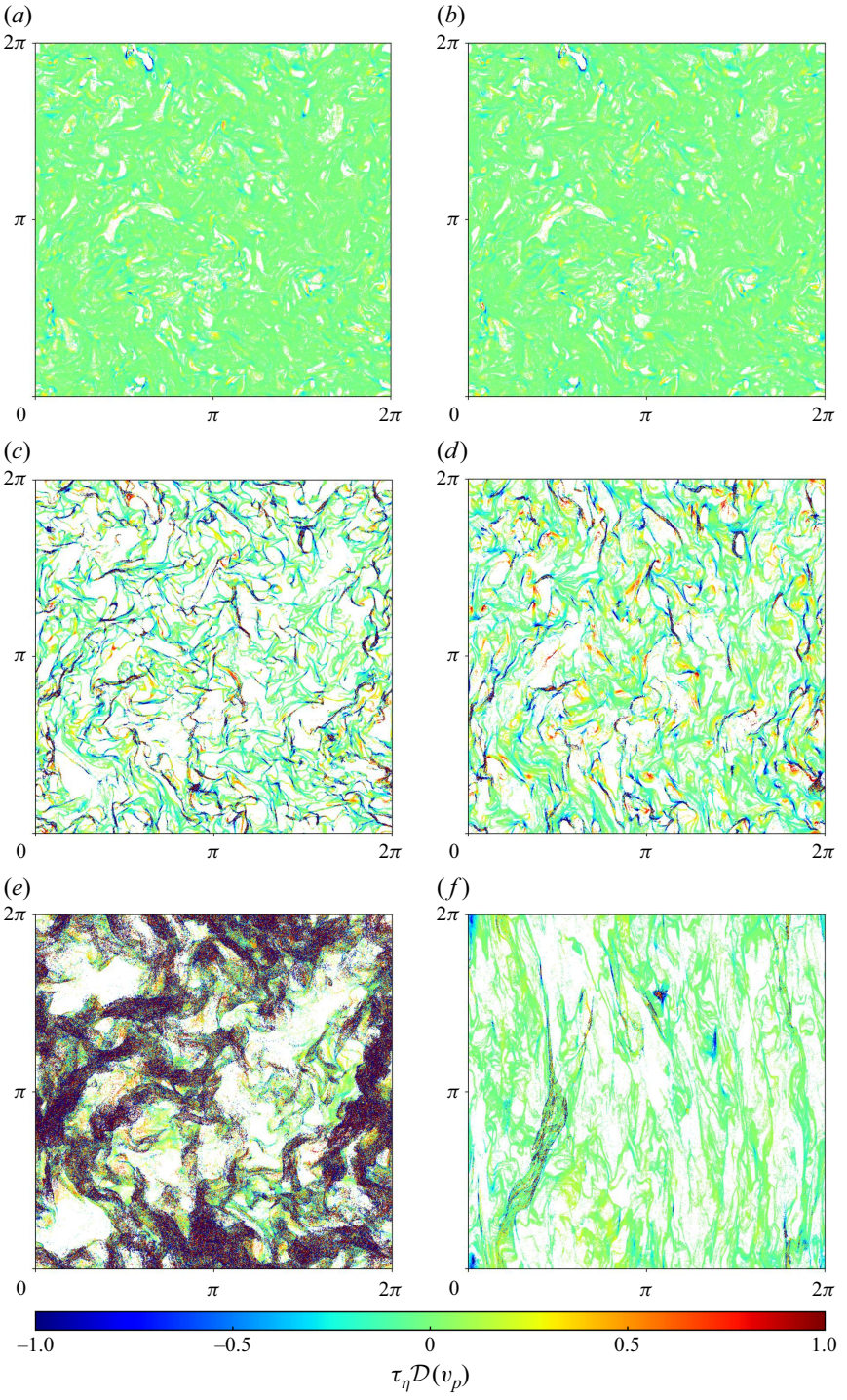

Figure 4. Two-dimensional slices of thickness $2\pi/1024$ in the yx-plane of the inertial particle positions coloured by the particle-velocity divergence $\mathcal{D}(\boldsymbol{v}_p)$ (a,c,e) without and (b,d,f) with gravity for (a,b) $St = 0.1$, (c,d) 1 and (e,f) $St = 5$.

turbulent interactions that typically drive convergence and divergence of particles. Overall, the observed patterns confirm previous studies (Bec *et al.* 2014; Gustavsson *et al.* 2014) and provide the physical context for the interpretation of the multiresolution analyses introduced below.

For high Stokes numbers without gravity in figure 4, we can observe cluster regions exhibiting both positive and negative divergence. The behaviour could explain the increase in variance for $St \geqslant 0.5$ as the Stokes number increases in the absence of gravity. This occurs when their inertial properties lead to more frequent crossing trajectories, i.e. the particle velocity becomes multivalued, which is referred to as caustics (Wilkinson & Mehlig 2005; Bec *et al.* 2010). Consequently, particles, on the whole, are more likely to converge or diverge strongly.

However, as this behaviour is more generalised, these events are statistically more frequent, resulting in a reduced flatness as observed in figure 3. In contrast, in the presence of gravity for $St > 1$, caustics are rarely observed (as illustrated in figure 4). When caustics do occur, they represent extreme deviations from typical fluctuations (i.e. the variance), thereby resulting in an increased flatness. It may be that, despite the overall damping effect of gravity, intermittent strong vortices occasionally cause particle clusters with distinct time histories to converge, leading to caustics.

These extreme divergence values originate from caustics. In phase space the particle dynamics evolves on a folded manifold, so that several velocity branches coexist at the same position. When this structure is projected onto configuration space ($\boldsymbol{x}$-space), particles on different branches approach the same location and cross with large relative velocities (Bec *et al.* 2024). In the idealised continuum description this collapse corresponds to the divergence of the particle-velocity field tending to $-\infty$ at the caustic (Meibohm *et al.* 2020) and then resuming from $+\infty$ immediately after crossing. In practice, such infinite values occur statistically only on sets of zero measure in configuration space, so that in a discrete particle system with a finite number of particles one observes very large but finite divergence values instead. This is analogous to the fact that, in one, two or three spatial dimensions, two points sampled from a continuous distribution coincide with probability zero. In a continuous-time description each particle trajectory is a one-dimensional curve in space–time, and in one spatial dimension (two-dimensional space–time) such curves can intersect with non-zero probability, whereas in two or three spatial dimensions their intersections occur only on sets of zero measure so that exact coincidences are not expected in a finite particle sample. Within particle clusters this process can occur almost simultaneously for many neighbouring particles, which produces the observed pattern of divergence alternating between large negative and large positive values at small scales.

We now aim to quantify observations made in figure 4 and assess the particle-velocity divergence at various scales. To this end, we apply the multiresolution analysis detailed in § 3.3, to the previously computed divergence. Figure 5 shows the wavelet energy spectrum of the particle-velocity divergence for different Stokes numbers, both in the absence and presence of gravity. The spectra are normalised by using the Kolmogorov scale η, the kinematic viscosity ν and the energy dissipation rate ϵ. The advantage of this method over the Fourier spectrum lies in its spatial locality, which is essential for capturing transient and localised events. Furthermore, the method operates on graphs, which represent the native structure of the data we work with, thereby eliminating the need to project the data onto a Cartesian grid for classical Fourier and wavelet analyses.

For $0.1 \leqslant St \leqslant 0.5$, the spectra show a peak around $k_V \eta \approx 0.5$. This means that the scale of cluster and void formation is almost the same for these Stokes numbers. Additionally, an increase in the Stokes number leads to an increase in the spectrum amplitude.

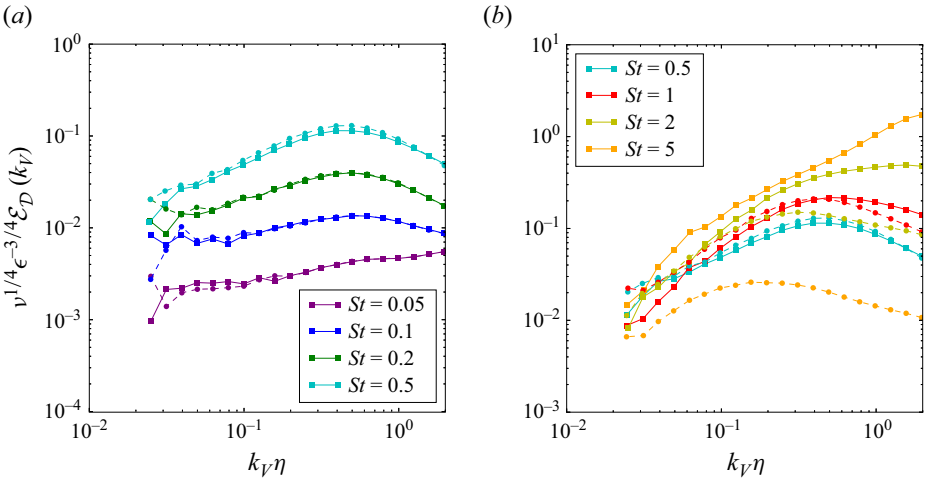

Figure 5. Wavelet energy spectrum of the particle-velocity divergence $\mathcal{E}_{\mathcal{D}}(k_V)$ for (*a*) small and (*b*) large Stokes number without (solid lines) and with (dashed lines) gravity.

This phenomenon could be linked to the increased particle relaxation time, as already discussed for figure 3. In contrast, for $St = 0.05$, the magnitude is much lower and no clear peak is observed at $k_V\eta \approx 0.5$. For such low inertia, the particle divergence is expected to be nearly zero, so the results at small scales are dominated by correlated numerical noise, as similarly observed when computing the divergence for $St = 0$ (Oujia *et al.* 2020). The decay of the spectrum at large wavenumbers is consistent with the fact that, for small Stokes numbers, relative velocities at small spatial separations remain weak (Bhatnagar, Gustavsson & Mitra 2018). As a result the particle-velocity field is smooth at the smallest scales and the divergence tends to vanish as the inter-particle separation goes to zero, so that little spectral energy is present at the largest wavenumbers.

In the cases of $St \geqslant 1$ without gravity, we can see that, as the Stokes number increases, the overall amplitude of the spectrum increases, and the wavenumber with the spectrum peak shifts to higher values, i.e. smaller scales. This behaviour can be attributed to the formation of caustics. When the velocity becomes multivalued, the divergence calculated using the tessellation-based method becomes noisy at small scales. As the range of values that the multivalued particle velocity can take expands, the amplitude of the spectrum at high wavenumbers also increases, due to the sampling, which creates discontinuities in the particle velocity. For the case $St = 5$ without gravity, although a decay is not apparent over the wavenumber range accessible in our data, this does not imply that the spectrum keeps increasing indefinitely toward smaller scales. Joint statistics of separations and relative velocities at comparable Stokes numbers show that large relative velocities at very small separations are possible but remain much less probable than small relative velocities (Bhatnagar *et al.* 2018). In the context of phase-space models (Bec *et al.* 2024), this corresponds to a regime where the phase-space correlation dimension D_2 remains below three, so that the second-order structure function of particle relative velocity, denoted $S_2(R)$, still tends to zero as the separation R tends to zero. Typical relative velocities therefore vanish at vanishing separation, even though rare caustic events produce large fluctuations of the relative velocity. In this situation, we expect the divergence spectrum to reach a maximum and then decrease at the largest wavenumbers, and the absence of a clear decay at $St = 5$ is most likely due to the finite number of particles and the limited range of resolved k_V. For even larger Stokes numbers, when D_2 exceeds three and

the spatial correlation dimension ($\hat{D}_2 = \min\{D_2, 3\}$) saturates at three, theory and model studies indicate that $S_2(R)$ approaches a constant as R tends to zero (Simonin *et al.* 2006; Bec *et al.* 2024). This regime of random uncorrelated motion corresponds to a divergence field that behaves like small-scale spatial noise in three dimensions, and in such a case the associated isotropic spectrum is not expected to decay at the largest wavenumbers, with its asymptotic scaling determined by the statistical properties of the underlying random field and one may conjecture a k_V^2 scaling at large wavenumbers.

In contrast, for $St \geqslant 1$ with gravity (i.e. $S_v \geqslant 6.79$), the general trend is a decrease in the overall amplitude of the spectrum when the Stokes number increases, and the wavenumber with peak shifts to lower values. This behaviour could be explained by the influence of gravity, which is conjectured to reduce the residence time of particles with large Stokes numbers within small vortices (Matsuda *et al.* 2017), thereby leading to fewer interactions with these structures. Thus, this weaker interaction with small-scale eddies reduces their contribution to the particle-velocity divergence, resulting in the peak shift toward larger scales.

4.3. *Rotation of particle velocity*

In this subsection, we investigate the curl of the particle velocity to understand how inertia and gravity affect the rotational behaviour of inertial particles. The curl of the particle velocity is computed using the method described in § 3.2. Studying the curl of the particle velocity provides insights into the vortical motion and the shearing behaviour in particle motion. In the gravity-free case, the behaviour of inertial particles is isotropic since we consider isotropic turbulence. Hence, we do not need to distinguish between coordinates in the gravity-free case. However, in the presence of gravity, the particle behaviour can be anisotropic. Therefore, we examine statistics separately for the curl component in the x-direction, i.e. in the same direction as gravity, and the curl components in both the y- and z-directions, i.e. perpendicular to the direction of gravity.

Figure 6 provides a quantitative measure of the variance and flatness of the curl of particle velocity $\boldsymbol{\mathcal{C}}(\boldsymbol{v}_p)$ normalised by the Kolmogorov time scale τ_η for different Stokes numbers. The corresponding PDFs are shown in Appendix B. In all cases, the variance and flatness are computed over the union of the sets of values corresponding to the individual curl components. In the absence of gravity, this union is formed by combining the x-, y- and z-component values. In the presence of gravity, however, only the horizontal components (i.e. the y- and z-components, which are statistically homogeneous) are merged, while the vertical x-component is treated separately. We observe that for $St \leqslant 0.2$, indicating a negligible impact of gravity, the variance slightly decreases while the flatness is almost constant. However, as the Stokes number increases further, we note that the variance increases in the absence of gravity, which is explainable by a more frequent occurrence of particle trajectory crossings. In contrast, in the presence of gravity, it increases from $St = 0.2$ to $St = 2$ (i.e. from $S_v = 1.36$ to $S_v = 13.6$) and then decreases, illustrating the impact of the gravity on the particle dynamics. This decay in variance for $St > 2$ is steep compared with the increase for $0.2 \leqslant St \leqslant 2$, and the variance value for $St = 5$ is significantly lower than that for all other considered Stokes numbers, even smaller ones like $St = 0.05$. Concerning the flatness, in the absence of gravity, flatness values increase from $St = 0.2$ to $St = 1$, and then decrease for higher values of St. Conversely, in the presence of gravity, flatness continues to increase for $St \geqslant 0.2$ (i.e. $S_v = 1.36$). The observed dependence of the flatness on the Stokes number can also be attributed to particle trajectory crossings. Indeed, the flatness of the curl appears to effectively quantify the intermittency associated with such crossing events. Furthermore, the variance and

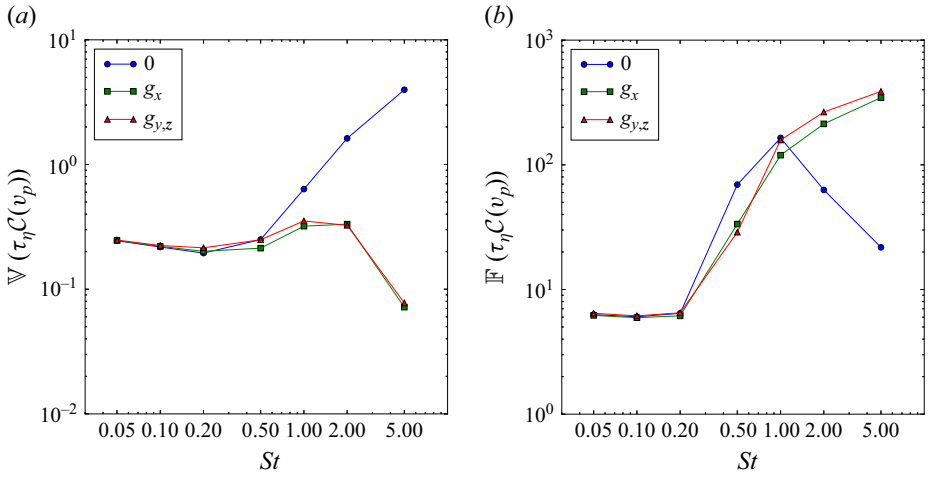

Figure 6. Variance $\mathbb{V}$ (a) and flatness $\mathbb{F}$ (b) of the curl the particle velocity $\boldsymbol{\mathcal{C}}(\boldsymbol{v}_p)$ normalised by the Kolmogorov time scale τ_η for different Stokes numbers without ($\boldsymbol{f}_g = \boldsymbol{0}$) and with ($\boldsymbol{f}_g = \boldsymbol{g}$) gravity in the x-direction ($\mathcal{C}_x(\boldsymbol{v}_p)$), and the y- and z-directions ($\mathcal{C}_{y,z}(\boldsymbol{v}_p)$).

flatness are slightly lower for the curl along the x-direction compared with those along the combined y- and z-directions for almost all considered Stokes numbers although the behaviour of these quantities is similar across the different directions.

Figure 7 presents the spatial distribution of particles in two-dimensional slices of the domain, coloured by particle enstrophy $\mathcal{Z}(\boldsymbol{v}_p)$, i.e. the squared norm of particle vorticity ($\mathcal{Z}(\boldsymbol{v}_p) = ||\boldsymbol{\mathcal{C}}(\boldsymbol{v}_p)||_2^2$), for three distinct Stokes numbers, for both cases, i.e. without and with gravity. For $St = 0.1$, enstrophy exhibits local fluctuations with significant variations between regions with strong rotation and those where particles are only transported. In regions where the particles are present, the enstrophy of inertial particles is similar to the enstrophy of fluid flow (e.g. see Maurel–Oujia *et al.* 2024), while the particles are not present in high enstrophy regions due to the centrifugal effect. This observation is consistent with the fact that particles continue to closely follow the fluid for this Stokes number. As expected, no significant difference can be observed between the cases without and with gravity. For $St = 1$, aside from the elongated clusters in the direction of gravity that we previously observed, difference in the enstrophy for the cases with or without gravity is not obvious in the visualisations. Conversely, for $St = 5$, a distinct difference can be observed in the magnitude of enstrophy between the cases without and with gravity. In particular, the value of enstrophy is significantly lower than that for the other considered Stokes numbers. In the gravity-free case, a similarity can be seen between the regions where the value of enstrophy is highest and the regions where the values of divergence oscillate, as shown in figure 4. This is due to the caustics, which are interpreted by the computational method as extreme values.

We aim to assess the curl of particle velocity across various scales of motion by applying the multiresolution analysis framework to the curl, aiming to quantify our observations from the preceding figure. Figure 8 presents the wavelet energy spectrum of the curl of the particle velocity for various Stokes numbers, illustrating particle behaviour both without and with gravity. Panel (a) depicts the scenario without gravitational influence, while panel (b) demonstrates the effects of gravity, analysed separately along the x-direction, and the y- and z-directions. Each curve represents an average of the various quantities considered. Specifically, in panel (a) we display $\mathcal{E}_{\mathcal{C}}(k_V) = (\mathcal{E}_{\mathcal{C}_x}(k_V) + \mathcal{E}_{\mathcal{C}_y}(k_V) + \mathcal{E}_{\mathcal{C}_z}(k_V))/3$, while

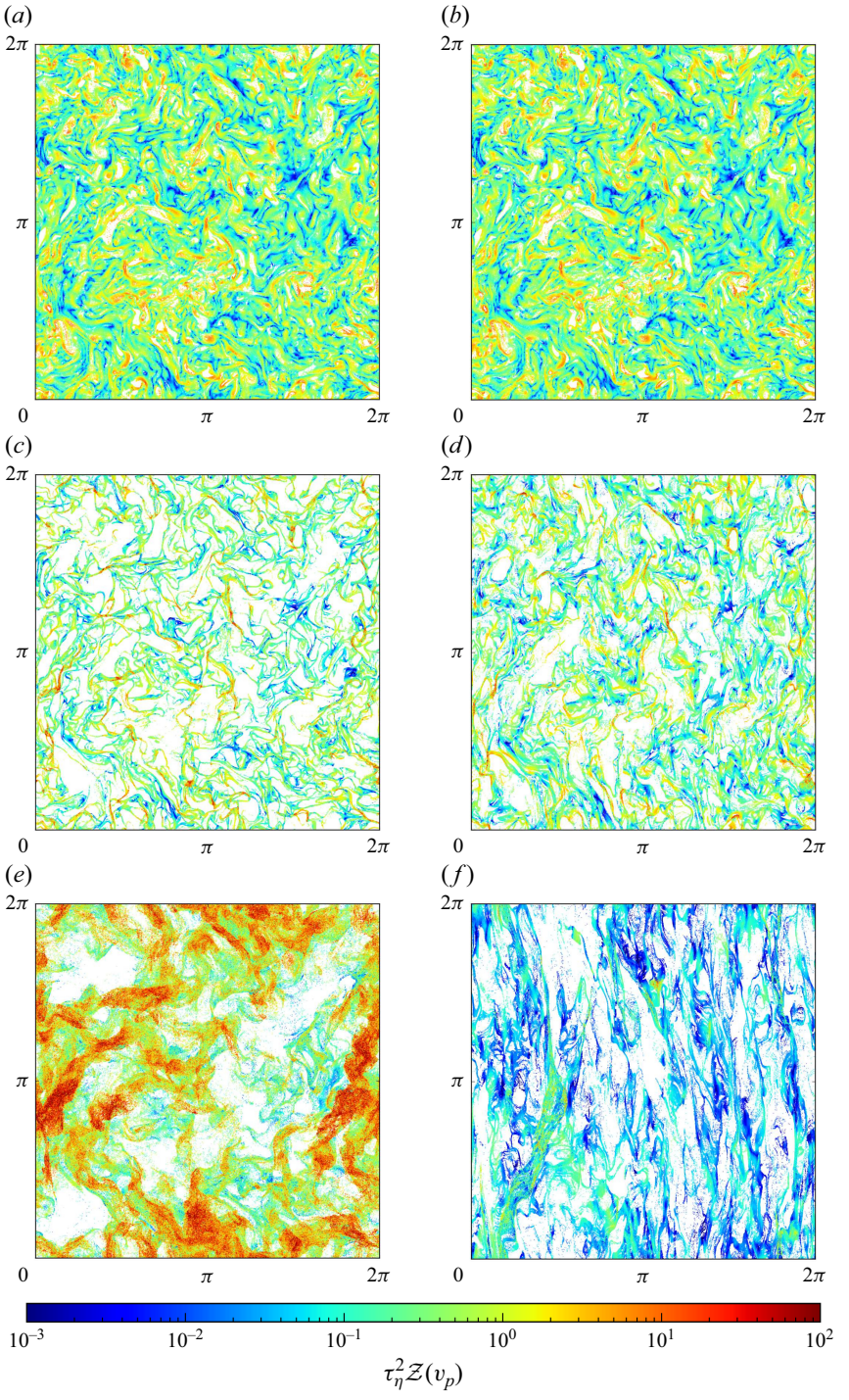

Figure 7. Two-dimensional slices of thickness $2\pi/1024$ in the yx-plane of the inertial particle positions coloured by the enstrophy of the particle velocity $\tau_\eta^2 \mathcal{Z}(\boldsymbol{v}_p)$ (*a*,*c*,*e*) without and (*b*,*d*,*f*) with gravity for (*a*,*b*) $St = 0.1$, (*c*,*d*) $St = 1$ and (*e*,*f*) $St = 5$.

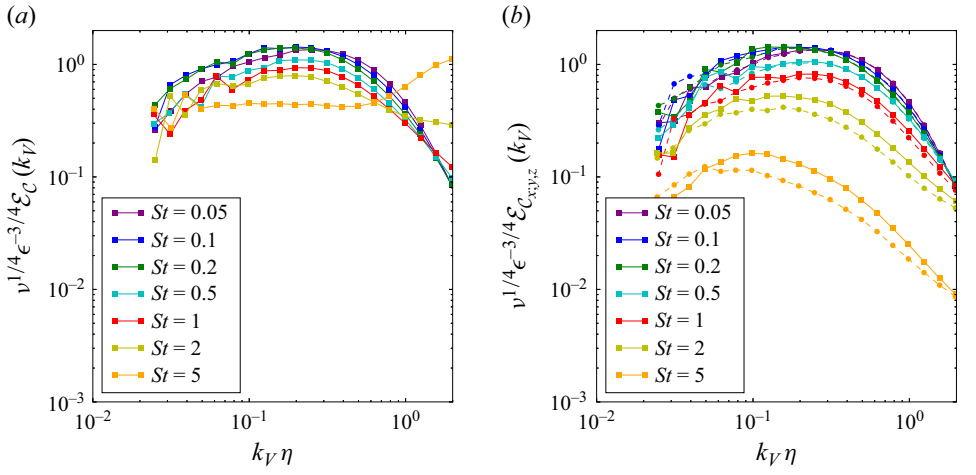

Figure 8. Wavelet energy spectrum of the curl of the particle velocity for different Stokes numbers: (*a*) the spectra $\mathcal{E}_{\mathcal{C}}(k_V)$ for the case without gravity and (*b*) the spectra for the case with gravity in the x-direction (solid lines) and in the y- and z-directions (dashed lines), $\mathcal{E}_{\mathcal{C}_x}(k_V)$ and $\mathcal{E}_{\mathcal{C}_{y,z}}(k_V)$, respectively.

in panel (*b*) the solid line corresponds to $\mathcal{E}_{\mathcal{C}_x}(k_V)$, and the dashed lines represent $\mathcal{E}_{\mathcal{C}_{y,z}}(k_V) = (\mathcal{E}_{\mathcal{C}_y}(k_V) + \mathcal{E}_{\mathcal{C}_z}(k_V))/2$. For small Stokes numbers, we observe a slight shift of the spectrum towards larger scales as inertia increases. Then, for $0.2 \leqslant St \leqslant 2$, there is a decrease in the peak value of the spectrum along with the increase in St. This decrease in the peak value of the spectrum is more significant in the presence of gravity up to $St = 5$. We can observe that, in the case with gravity, the peak value is slightly larger in the x-direction than in the y- and z-directions, while the opposite can be observed for small wavenumbers. In the scenario without gravity, there is also a notable increase in the higher wavenumbers as the Stokes number increases for $St \geqslant 0.5$, which is due to particle crossings and random behaviour of the particles. This is particularly visible for $St = 5$, as we had already observed in figure 7. Thus, in the case without gravity, we observe that rotational motion at scales corresponding to $k_V\eta \approx 0.5$ diminishes as the Stokes number increases. For $St = 5$, it is noted that the majority of the contribution to the PDF of the curl of the particle velocity in figure 15(*a*) is due to small scales, which are attributable to caustics. In the case with gravity, we observe a decrease in the amplitude of the wavelet energy spectrum. Particles tend to be advected mainly in the direction of gravity at a relatively spatially uniform speed across different regions of the domain. This results in shear reduction of the particle velocity, and thus in reduced enstrophy values at all scales.

4.4. *Helicity of particle velocity*

In this subsection, we analyse the relative helicity of the particle velocity to discern the underlying swirling motion of inertial particle-laden turbulent flow and to understand the nature of particle motion influenced by forces such as inertia and gravity. The study of helicity provides insights into coherent or incoherent particle motion and is considered a topological statistics. Large helicity values, i.e. strong alignment or anti-alignment between velocity and vorticity, tend to suppress chaotic mixing and lead to swirling three-dimensional motion. Thus helicity can be seen as a measure of flow organisation. In this work, we refer to coherent particle motion as the coordinated, non-random motion of a group of particles (a particle and its neighbours, or clusters) that forms structures persisting in time and space. In such regions, particle related quantities, such as particle velocity,

vorticity, divergence or helicity, exhibit weak fluctuations within the group, in contrast to the strongly irregular variations expected for random particle motion.

Rewriting the incompressible Euler equations in terms of the Lamb vector reveals that nonlinearity decreases when the velocity aligns with the vorticity, corresponding to a relative helicity of -1 or 1. This alignment between these two quantities simplifies the flow motion. Moreover, in incompressible flows it has been observed that vortex tubes often maximise helicity (Tsinober & Levich 1983; Levich 1987). In Farge, Pellegrino & Schneider (2001), helicity is utilised to identify vortex tubes and to distinguish between coherent structures and incoherent motion within the flow. It is observed that the PDF of the relative helicity of the coherent flow exhibits a convex shape with two pronounced maxima at -1 and 1, while the incoherent flow has a concave shape with a maximum at 0. In this section, we will adopt a similar approach for helicity of the particle flow. The relative helicity plays the same role even for coherent particle flows when the flows are close to continuous since the particle momentum equation obtained from the Boltzmann equation has a similar form to the Navier–Stokes equation (Kasbaoui *et al.* 2019). However, the same idea may not be applicable when the effect of random particle motions exceeds the effect of the nonlinear transport relevant to the Lamb vector. Therefore, the relative helicity may not be an appropriate indicator of coherent structure in the caustic regions.

Unlike divergence or curl, helicity is not Galilean invariant. When a uniform mean velocity is applied to the entire flow field, the helicity value changes. We can express the particle velocity as $\boldsymbol{v}_p = \boldsymbol{v}'_p + \overline{\boldsymbol{v}}_p$, where $\boldsymbol{v}'_p$ represents the fluctuating component of the particle velocity and $\overline{\boldsymbol{v}}_p$ is the mean particle-velocity vector. For the case without gravity, $\overline{\boldsymbol{v}}_p$ is statistically zero vector since the particle motion is affected only by the HIT, whereas for the case without gravity, $\overline{\boldsymbol{v}}_p$ deviates from zero vector due to the gravitational settling velocity. When $\overline{\boldsymbol{v}}_p \neq \boldsymbol{0}$, we have

$$\mathcal{H}(\boldsymbol{v}_p) = \frac{\boldsymbol{v}_p \cdot \boldsymbol{\mathcal{C}}(\boldsymbol{v}_p)}{||\boldsymbol{v}_p||_2 \, ||\boldsymbol{\mathcal{C}}(\boldsymbol{v}_p)||_2} \tag{4.1}$$

$$= \frac{\boldsymbol{v}'_p \cdot \boldsymbol{\mathcal{C}}(\boldsymbol{v}'_p) + \overline{\boldsymbol{v}}_p \cdot \boldsymbol{\mathcal{C}}(\boldsymbol{v}'_p)}{||\boldsymbol{v}'_p + \overline{\boldsymbol{v}}_p||_2 \, ||\boldsymbol{\mathcal{C}}(\boldsymbol{v}'_p)||_2} \neq \mathcal{H}(\boldsymbol{v}'_p). \tag{4.2}$$

For this reason, in the case with gravity, we have also computed the relative helicity $\mathcal{H}(\boldsymbol{v}'_p)$ after subtracting the mean particle velocity in the x-direction from the particle velocity, in addition to $\mathcal{H}(\boldsymbol{v}_p)$.

Figure 9 shows the PDFs of the relative helicity of particle velocity for various Stokes numbers, both without and with gravity. As the impact of gravity is very low, no significant change is expected. In the gravity-free scenario, as the Stokes number increases, the PDF shape becomes more convex, exhibiting two distinct maxima a ± 1. In Farge *et al.* (2001), this pattern was shown to be characteristic of coherent structures in fluid turbulence. This suggests that similar conclusions can be drawn for the motion of inertial particles, i.e. this pattern indicates coherent structures in the motion of inertial particles. A transition occurs at $St = 2$, where the PDF shape shifts from convex to concave shape. At $St = 5$, the PDF becomes concave, showcasing a maximum at 0 and two minima at ± 1. This distribution implies that the vorticity is more likely to be orthogonal to the particle velocity at higher Stokes numbers, suggesting a predominantly two-dimensional particle motion, i.e. the flow is only weakly swirling. This pattern is indicative of incoherent motion in fluid turbulence (Farge *et al.* 2001), and by analogy, similar conclusions can be applied to the motion of inertial particles.

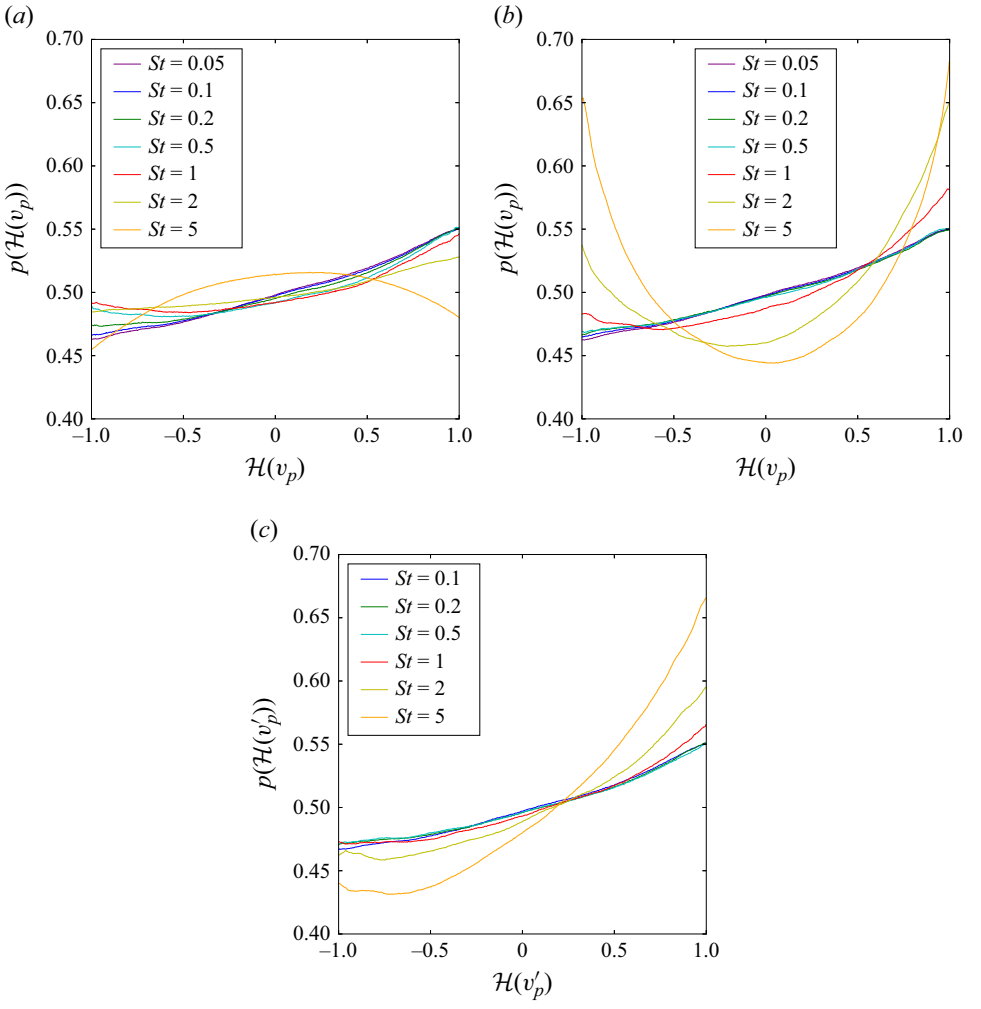

Figure 9. The PDFs of the relative helicity $\mathcal{H}(\boldsymbol{v}_p)$ of the particle velocity for different Stokes numbers (*a*) without and (*b*) with gravity and (*c*) the relative helicity $\mathcal{H}(\boldsymbol{v}'_p)$ of the particle-velocity fluctuation for the case with gravity.

In figure 9(*b*), we can observe that particle motion is strongly helical for the larger Stokes numbers. This is consistent with the results shown in figure 8, where the magnitude of x-component of the curl is higher compared with the other directions. Given that the mean particle velocity is also oriented along the x-direction due to gravity, it is expected that we observe a greater alignment between velocity and vorticity vectors, resulting in higher helicity values.

This behaviour is reduced in figure 9(*c*) where the mean particle velocity has been subtracted, although the motion remains helical. While in the gravity-free case, the PDF tended to become concave and the motion more two-dimensional for the larger Stokes numbers studied, in the presence of gravity, the relative helicity exhibits increasingly helical behaviour as the Stokes numbers increase, even for $St = 5$. This suggests that particles tend to exhibit swirling motion as they fall. The influence of gravity, therefore,

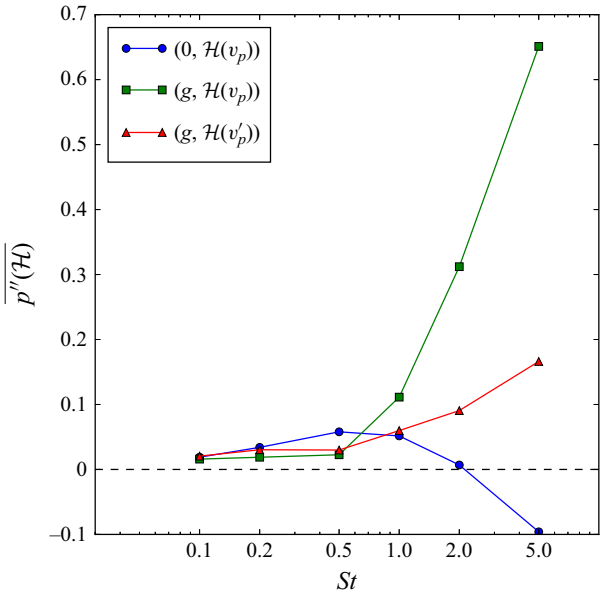

Figure 10. Average of the second derivative of the PDF of the relative helicity $\mathcal{H}(\boldsymbol{v}_p)$ for different Stokes numbers without ($\boldsymbol{0}$, $\mathcal{H}(\boldsymbol{v}_p)$) and with gravity without modification ($\boldsymbol{g}$, $\mathcal{H}(\boldsymbol{v}_p)$) and by removing the mean particle velocity in the x-direction ($\boldsymbol{g}$, $\mathcal{H}(\boldsymbol{v}'_p)$).

appears to enhance the coherence in the particle motion, leading to more helical flow patterns, particularly at higher Stokes numbers.

These various observations can be quantified in figure 10, which presents the average values of the second derivative of the PDF of relative helicity, i.e.

$$\overline{p''(\mathcal{H})} = \int_{-1}^{1} \frac{d^2 p(\mathcal{H})}{\mathrm{d}\mathcal{H}^2} \mathrm{d}\mathcal{H}. \tag{4.3}$$

This quantity permits assessment of the convexity of the PDF curves, thereby enabling a quantitative evaluation of the coherent or incoherent motion of the particles. Curve smoothing was applied using the Savitzky–Golay algorithm (Savitzky & Golay 1964) before computing the second derivative of each PDF curve. A value close to zero indicates a curve with a linear shape, a positive value denotes a convex curve and a negative value signifies a concave curve. For $St = 0.1$, the value of convexity is positive but low. In the case without gravity, we can observe an increase in convexity with a maximum value at $St = 0.5$, followed by a decay until $St = 5$ where the value becomes negative, with the highest amplitude among all Stokes numbers considered in the absence of gravity. In the case with gravity, there is no observed decrease in convexity, reaching a maximum at $St = 5$. In the case with gravity, with the mean particle velocity subtracted, the convexity also increases but not as strongly compared with not subtracting the mean particle velocity. We can also note that the convexity values for $St = 0.2$ and $St = 0.5$ are similar, which is further reflected by the fact that the PDFs are almost superimposed.

To further assess the coherence of particle motion and to clarify the role of caustics in shaping the relative helicity statistics, we complement the PDF based analysis with spatial visualisations and conditional probabilities of helicity. Figure 11 shows the spatial distribution of particles in two-dimensional slices of the domain, coloured by the relative helicity associated with the fluctuating particle velocity. Unlike the divergence and

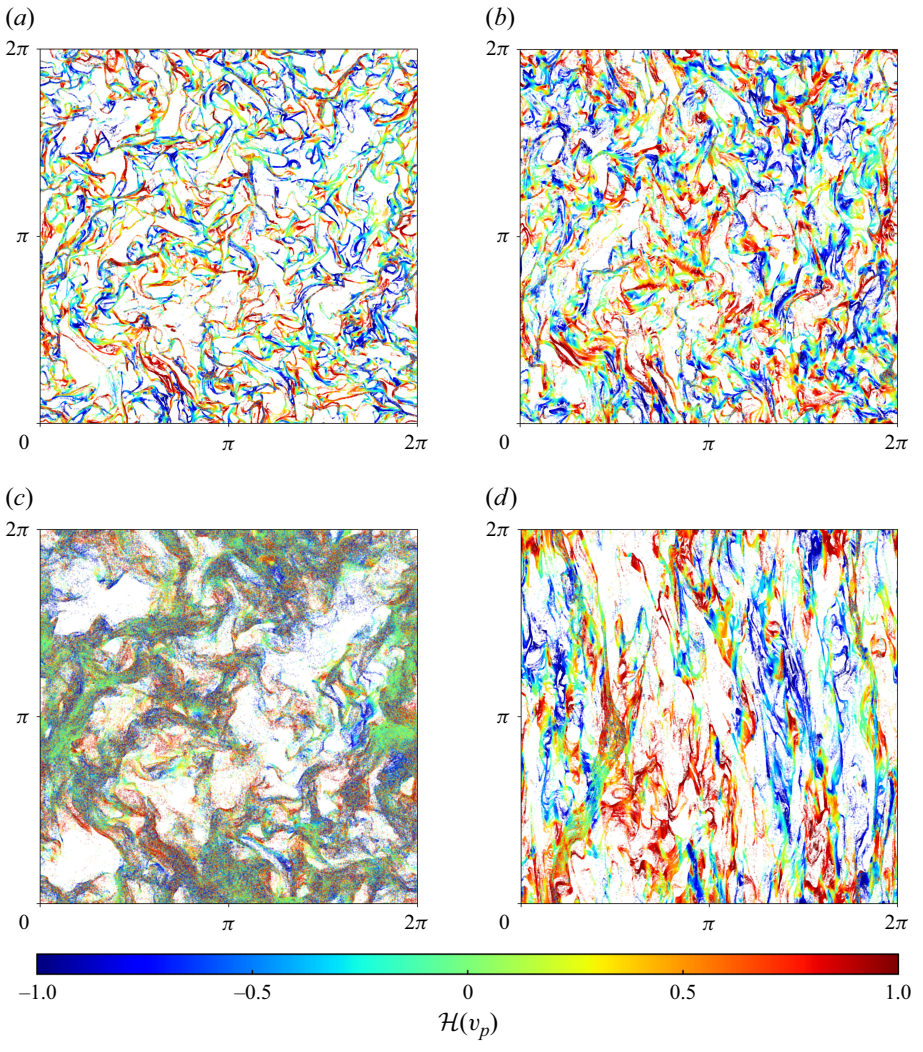

Figure 11. Two-dimensional slices of thickness $2\pi/1024$ in the yx-plane of the inertial particle positions coloured by the relative helicity of the fluctuating particle velocity (*a*,*c*) without and (*b*,*d*) with gravity for (*a*,*b*) $St = 1$ and (*c*,*d*) $St = 5$.

enstrophy visualisations, we do not show the low-inertia case (e.g. $St = 0.1$) since we focus on regimes where a difference between the cases without and with gravity becomes visible. We can observe that, except for the case $St = 5$ without gravity, helicity exhibits spatially continuous fluctuations, with progressive variations from one particle to another in regions where particles are present. We also find that, except for $St = 5$ without gravity, the majority of particle clusters has large helicity magnitude values which means that they exhibit swirling motion. This is particularly interesting for the case $St = 5$ with gravity where strong helicity magnitude indicates that the settling of heavy particles takes place in a swirling motion. Conversely, for $St = 5$ without gravity, we observe a strong intermittency of helicity, with abrupt variations, including changes in sign and amplitude, for particles that are close to each other. This intermittency is nevertheless not uniform throughout the domain, and some regions instead show smoother variations, comparable to

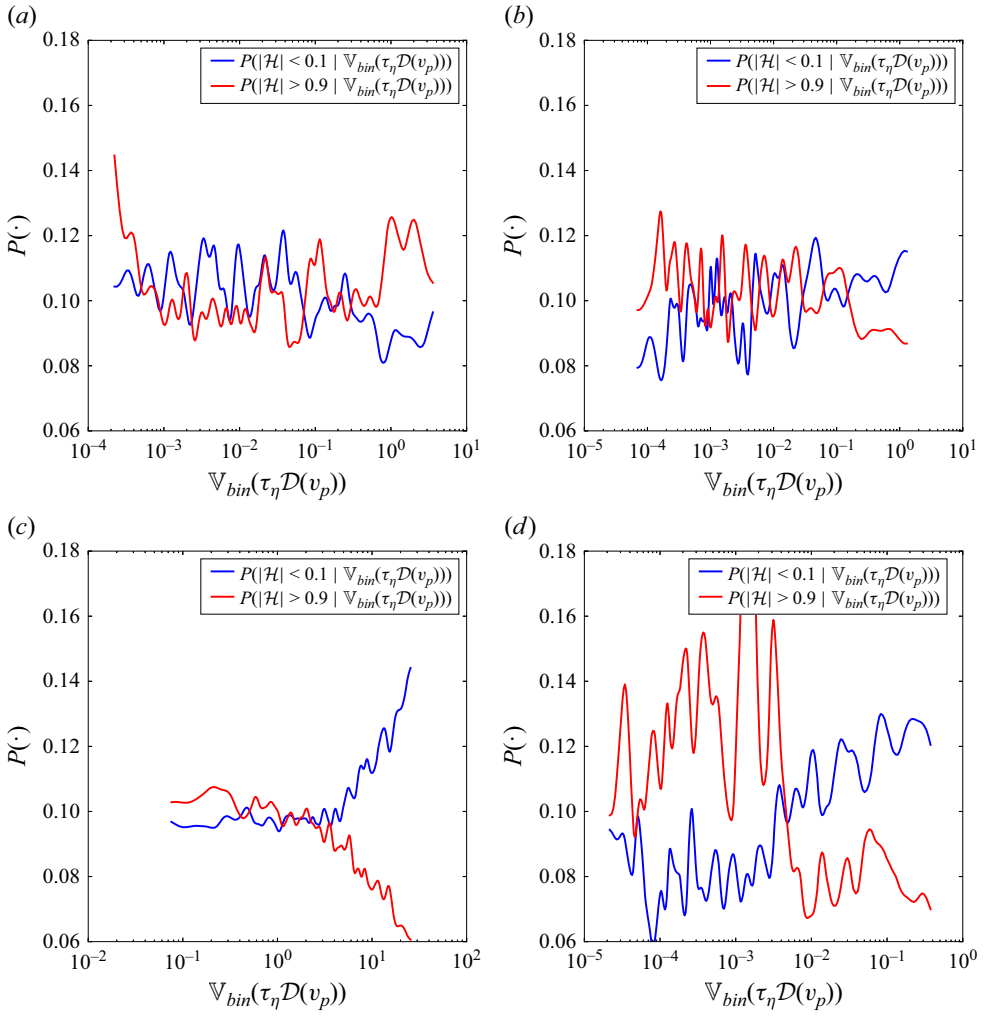

Figure 12. Conditional probabilities of observing a low relative helicity $|\mathcal{H}| < 0.1$ (blue lines) and a high relative helicity $|\mathcal{H}| > 0.9$ (red lines) as a function of the local variance of the particle-velocity divergence (used here as a proxy to identify caustic regions), $\mathbb{V}_{bin}(\tau_\eta \mathcal{D}(\boldsymbol{v}_p))$, evaluated in spatial bins on the yx-plane using a 512×512 grid for particles belonging to a slice of thickness $2\pi/1024$. The probabilities are estimated by grouping particles into 256 variance quantile bins, and the curves are smoothed for readability using a Gaussian filter with $\sigma = 3.0$. Results are shown (*a*,*c*) without and (*b*,*d*) with gravity for (*a*,*b*) $St = 1$ and (*c*,*d*) $St = 5$.

those observed for the other parameters. By comparing the helicity distribution for $St = 5$ without gravity (figure 11*c*) with the corresponding divergence visualisation (figure 4*e*) we observe that the regions where helicity is the most intermittent coincide with regions where divergence exhibits intense oscillations that are characteristic of caustics. Conversely, the continuous transitions of helicity correspond to regions where these caustic signatures are absent or weak. A similar correspondence, although less pronounced, can also be observed for the other cases by comparing with the corresponding divergence figure. We predict that, when helicity is intermittent in caustic dominated regions, it should also exhibit strong temporal fluctuations. In particular, during trajectory crossing events associated with caustics, the local helicity carried by the particles is expected to vary

rapidly, indicating that it is not temporally stable in those regions. However, the fact that helicity becomes intermittent in caustic regions does not provide information on the impact of caustics on the helicity distribution.

To quantify the impact of caustics on helicity, we relate the relative particle helicity to local divergence fluctuations, using the variance of $\tau_\eta \mathcal{D}(\boldsymbol{v}_p)$ as a proxy to localise regions dominated by caustics. We discretise the yx-plane on a regular 512×512 grid and within each bin we compute the variance $\mathbb{V}_{bin}(\tau_\eta \mathcal{D}(\boldsymbol{v}_p))$ from the values carried by the particles located in that bin. Each particle is then assigned the variance of the bin that contains it. Figure 12 shows, for $St = 1$ and $St = 5$ and for the cases without and with gravity, the conditional probabilities of observing a low relative helicity $P(|\mathcal{H}| < 0.1|\mathbb{V}_{bin}(\tau_\eta \mathcal{D}(\boldsymbol{v}_p)))$ and a high relative helicity $P(|\mathcal{H}| > 0.9|\mathbb{V}_{bin}(\tau_\eta \mathcal{D}(\boldsymbol{v}_p)))$ as a function of $\mathbb{V}_{bin}(\tau_\eta \mathcal{D}(\boldsymbol{v}_p))$. These probabilities are estimated by grouping particles into 256 classes defined by variance quantiles and then computing within each class the fraction of particles satisfying each threshold. The curves are smoothed using a Gaussian filter with parameter $\sigma = 3.0$ to improve readability. If caustics had no impact on helicity, we would expect to observe a constant curve, up to statistical noise. We can observe that, for $St = 1$ without and with gravity, indeed no clear trend emerges, as the statistics are dominated by noise due to the limited number of samples. Conversely, for $St = 5$, a trend appears in the evolution of both probabilities. This trend is clear in the case without gravity. More precisely, the probability of observing a low relative helicity increases with the divergence variance, and thus with caustic intensity, whereas the probability of observing a high relative helicity decreases as the divergence variance increases.

5. Conclusions

In this work we studied the behaviour of one-way coupled inertial particle-laden homogeneous isotropic turbulent flows over a range of Stokes numbers ($0.05 \leqslant St \leqslant 5$) at a Taylor-microscale Reynolds number $Re_\lambda = 204$. Simulations were conducted both with and without gravitational settling. In the former case, the Froude number was fixed at $Fr = 0.145$. We applied a novel tessellation-based methodology to quantify and to analyse the multi-scale properties of particle velocity, including its divergence, curl, helicity and their corresponding energy spectra. This approach provided a deeper understanding of the nuanced dynamics governing inertial particle-laden flows. The graph-based multiresolution analysis provides quantitative insight into the scale distribution of the particle-velocity divergence and curl, and it shows in particular that gravitational settling shifts the dominant activity toward larger scales, whereas in the absence of gravity caustics increasingly concentrate the activity at smaller scales for large St. In addition, the helicity analysis indicates that, at high St, gravitational settling is associated with more pronounced coherent swirling motion, with increased alignment and anti-alignment between the particle velocity and the particle vorticity.

Throughout this investigation, we observed that for small Stokes numbers ($St \leqslant 0.2$, equivalent to $S_v \leqslant 1.36$ in this work), as expected from many past studies, there is no significant difference between scenarios without and with gravity in terms of their distribution or dynamic behaviour concerning divergence, curl or helicity. This indicates that gravitational effects are negligible in this low-inertia regime with small settling velocity. In our results, differences between the cases without and with gravity become perceptible for $S_v = 3.39$ ($St = 0.5$ for $Fr = 0.145$), and are clearly visible for $S_v = 6.79$ ($St = 1$). This is consistent with the expectation that changes become significant once $S_v = \mathcal{O}(1)$. For comparison, Ireland *et al.* (2016*b*) report that the influence of gravity on relative particle velocities, which provides a useful proxy for gauging the strength of

settling effects, is less apparent at weak settling, $S_v = 5.79$ ($St = 0.3$ in their $Fr = 0.052$ dataset), whereas it becomes pronounced for $S_v = 19.3$ ($St = 1$).

The particle distribution undergoes significant transformations as the Stokes number increases. By examining the volume distribution in the absence of gravity, we observe more pronounced clusters and void regions as the Stokes number increases up to $St = 1$, while particles become more dispersed for $St > 1$. Conversely, in the presence of gravity, void regions persist even for $St \geqslant O(1)$, indicating that gravity sustains these inhomogeneities for larger inertia. This may be because gravitational settling reduces trajectory crossings associated with caustics and the resulting small-scale mixing, which otherwise tend to weaken the contrast between clusters and voids at large St.

Consistent with previous studies, our results confirm that the spatial structures of the particle dynamics are significantly altered by gravity. Here, we further quantify how the associated modifications in clustering and void formation are reflected in the particle-velocity divergence. In the absence of gravity, particles at higher Stokes numbers exhibit more frequent crossing trajectories and multivalued velocities (corresponding to caustics), resulting in highly variable convergence and divergence values at small scales. In contrast, gravitational settling can modify the prevalence of caustics and the associated small-scale variability, consistent with analyses of how the caustic formation rate depends on gravity (Gustavsson *et al.* 2014). At the same time, particle inertia acts as a low-pass filter of the carrier flow velocity, which reduces the contribution of the smallest turbulent fluctuations to the particle velocity. Statistical analyses confirm that for large Stokes numbers the intermittency of the particle flow increases. The wavelet energy spectrum of the particle-velocity divergence shows that the amplitude of divergence increases with the Stokes number for $St \leqslant 1$, due to the increase in inertia and hence the creation and destruction of void regions. As the Stokes number increases beyond $St = 1$, without gravity, the peak of the divergence spectrum shifts toward higher wavenumbers ($k_V \eta > 0.5$), corresponding to smaller spatial scales, while with gravity, the peak shifts toward lower wavenumbers ($k_V \eta < 0.5$), associated with larger spatial scales. Gravity thus appears to lead to more moderate fluctuations across the flow domain and to a relative reduction in the smallest-scale variability of particle behaviour.

For the curl of the particle velocity, a significant change occurs as the Stokes number increases. When $St \leqslant 0.2$ and in the absence of gravity, the variance of the curl slightly decreases. This behaviour suggests that particles, which are still closely following the flow due to their low inertia, tend to concentrate in regions of lower vorticity. As St increases beyond 0.2 and without gravity, the variance of the curl rises with increasing Stokes number, reflecting the enhanced inertial effects and the influence of turbulent structures on the particle behaviour. The introduction of gravity modifies this behaviour for $St > 0.2$: the variance increases with St more gently than without gravity, and it shows a maximum at $St = 2$. For $St = 5$, the variance is significantly lower than at all other considered Stokes numbers.

The analysis of relative helicity indicated that, as St approached one, the particle motion increasingly adopts swirling motion. In the absence of gravity, this behaviour changes with an increase in inertia towards quasi two-dimensional particle motion, i.e. absence of swirl, whereas in the presence of gravity, the behaviour continues to become more helical, suggesting organisation into more coherent particle motion.

These findings highlight a transition from relatively erratic to more coherent behaviour as gravitational effects become pronounced, particularly at higher Stokes numbers, elucidating the effects of inertia, gravity and turbulence. In our study, we focused on the influence of the Stokes number and gravity, with a fixed Froude number, on the particle

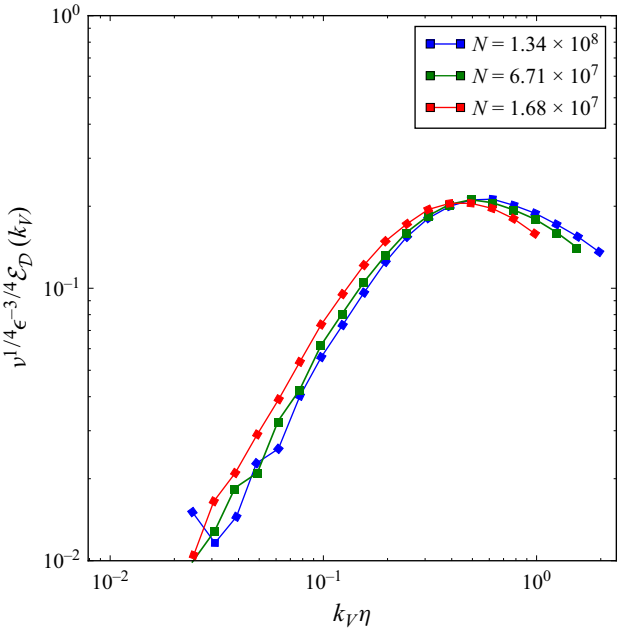

Figure 13. Wavelet energy spectrum of the particle-velocity divergence of inertial particles in HIT for $Re_\lambda = 204$, $St = 1.0$ computed for different number of particles $N_p = 1.68 \times 10^7$, 6.71×10^7 and 1.34×10^8.

dynamics. Future investigations of the particle dynamics across varying Froude numbers could provide valuable insights into particle behaviour.

A perspective for a possible low-order description of particle-laden flows is the coherent cluster extraction, proposed in (Bassenne *et al.* 2017). Wavelet analysis, in the present work generalised for point particles leading to multiresolution analysis on graphs, has been used to extract coherent clusters applying thresholding to the wavelet coefficients. It was shown that few per cent of the wavelet coefficients ($< 2\,\%$) can represent the clusters and thus yield an efficient representation of the particle number-density field with a corresponding non-uniform adaptive computational grid. This can then be useful for instance to compute radiative transfer in particle-laden flow, e.g. with application in atmospheric dust clouds.

Acknowledgements. The DNS and data analyses for this project were performed using the Earth Simulator supercomputer system of JAMSTEC. T.M.O. acknowledges support from the JSPS International Research Fellowships for Research in Japan (Short-term).

Funding. T.M.O. and K.S. acknowledge funding from the Agence Nationale de la Recherche (ANR) under grant ANR-20-CE46-0010-01. K.M. acknowledges financial support from JSPS KAKENHI under grant numbers JP20K04298 and JP23K03686.

Declaration of interests. The authors report no conflict of interest.

Appendix A. Effect of the number of particles

Figure 13 shows the wavelet energy spectrum of the particle-velocity divergence computed from DNS data, for $St = 1$ without gravity considering different numbers of particles $N_p = 1.68 \times 10^7$, 6.71×10^7 and 1.34×10^8. We can observe that the spectrum retains the

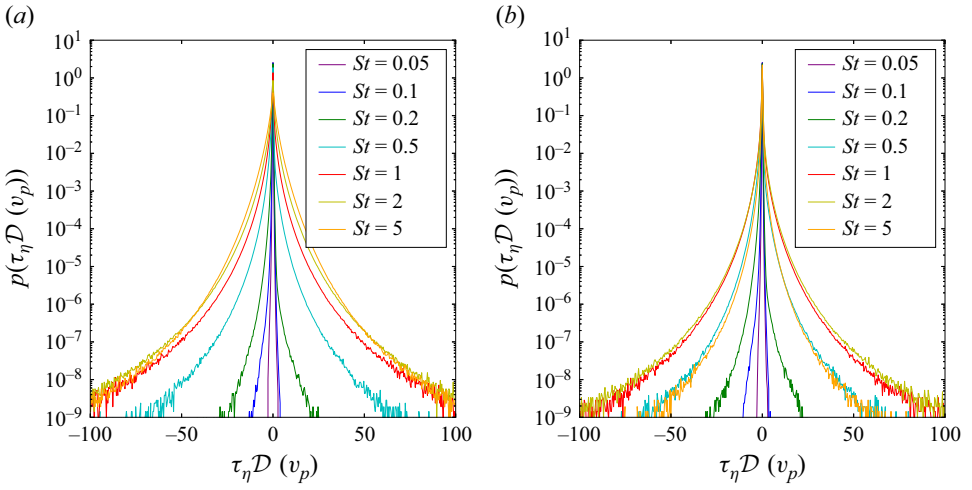

Figure 14. The PDFs of the particle-velocity divergence $\mathcal{D}(\boldsymbol{v}_p)$ for different Stokes numbers (*a*) without and (*b*) with gravity, normalised by the Kolmogorov time scale τ_η.

same shape but is shifted towards larger wavenumbers, i.e. smaller scales, as the number of particles increases. This is consistent with the nature of one-way coupled inertial particles. Indeed, as their number increases, the size of the cell volumes decreases, which is represented by the higher values of k_V. Furthermore, it is expected that the shape of the spectrum does not change since the increasing number of particles does not influence the behaviour of the flow.

Appendix B. Probability density function of divergence and curl

Figure 14 shows the PDFs of the particle-velocity divergence $\mathcal{D}(\boldsymbol{v}_p)$ normalised by the Kolmogorov time scale τ_η for various Stokes numbers, both without and with the influence of gravity. The PDFs have a stretched exponential shape. In the absence of gravity, the probability of having high positive or negative divergence values increases with the Stokes number and then saturates for $St > 1$. In the presence of gravity, the PDF of divergence shows a similar pattern to the non-gravity case for $St \leqslant 2$, but the probability of observing large positive or negative values decreases at $St = 5$.

Figure 15 shows the PDFs of the curl $\boldsymbol{\mathcal{C}}(\boldsymbol{v}_p)$ of the particle velocity for various Stokes numbers, detailing the effects without gravity (*a*) and with gravity on different directions: the x-component (*b*), and the combined y- and z-components (*c*). Here, $\mathcal{C}_{y,z}(\boldsymbol{v}_p)$ denotes the union of the y- and z-component distributions of the particle-velocity curl. The PDFs illustrate how the Stokes number and the presence of gravity influences the rotational motion of particles in the flow. The behaviour of the PDFs is similar to that of the PDFs of divergence, i.e. the probability of high positive or negative divergence values increases with the Stokes number for $0.2 \leqslant St \leqslant 2$ in both the absence and presence of gravity. It shows saturation in the absence of gravity and a reduction in the extreme values in the presence of gravity for $St > 2$.

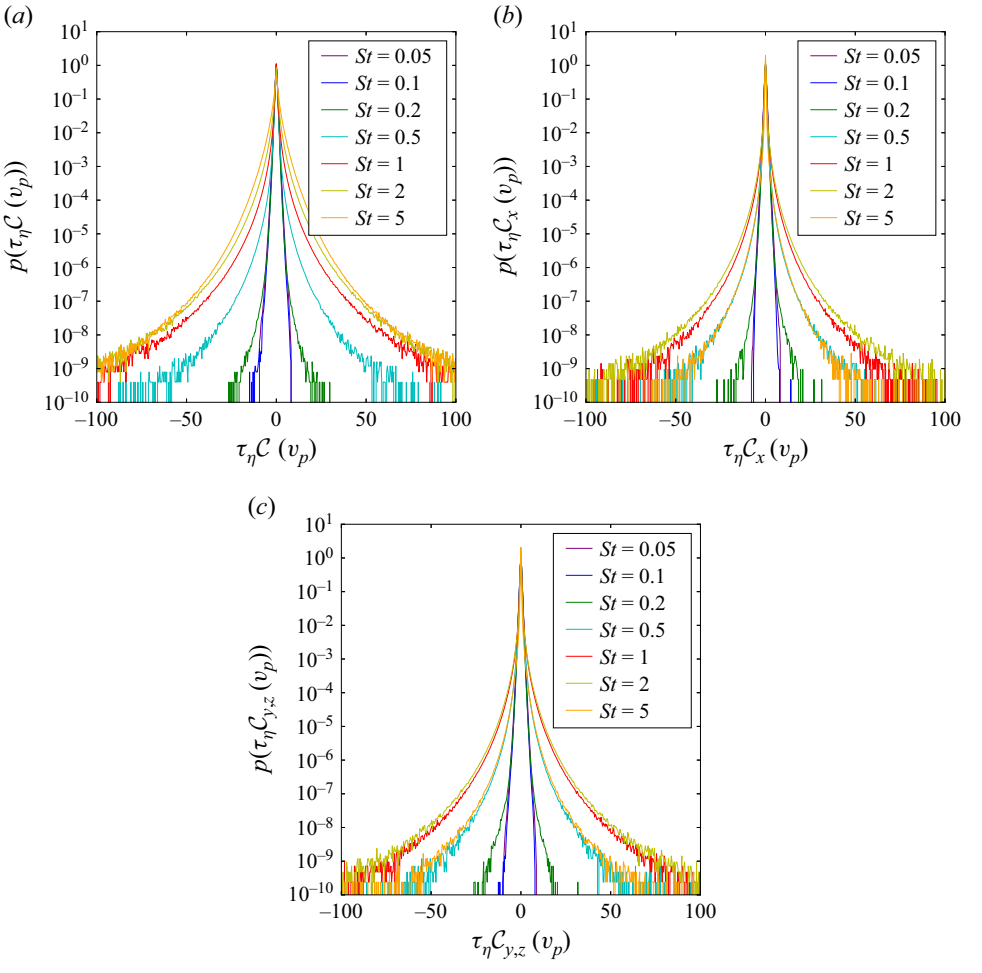

Figure 15. The PDFs of the curl $\mathcal{C}(\boldsymbol{v}_p)$ of the particle velocity for different Stokes numbers (*a*) without and (*b*,*c*) with gravity in the (*b*) x-direction, and (*c*) the y- and z-directions.

References

Apte, S.V., Oujia, T., Matsuda, K., Kadoch, B., He, X. & Schneider, K. 2022 Clustering of inertial particles in turbulent flow through a porous unit cell. *J. Fluid Mech.* **937**, A9.

Baker, L., Frankel, A., Mani, A. & Coletti, F. 2017 Coherent clusters of inertial particles in homogeneous turbulence. *J. Fluid Mech.* **833**, 364–398.

Bassenne, M., Urzay, J., Schneider, K. & Moin, P. 2017 Extraction of coherent clusters and grid adaptation in particle-laden turbulence using wavelet filters. *Phys. Rev. Fluids* **2** (5), 054301.

Bec, J., Biferale, L., Cencini, M., Lanotte, A.S. & Toschi, F. 2010 Intermittency in the velocity distribution of heavy particles in turbulence. *J. Fluid Mech.* **646**, 527–536.

Bec, J., Gustavsson, K. & Mehlig, B. 2024 Statistical models for the dynamics of heavy particles in turbulence. *Annu. Rev. Fluid Mech.* **56** (1), 189–213.

Bec, J., Homann, H. & Ray, S.S. 2014 Gravity-driven enhancement of heavy particle clustering in turbulent flow. *Phys. Rev. Lett.* **112** (18), 184501.

Bhatnagar, A., Gustavsson, K. & Mitra, D. 2018 Statistics of the relative velocity of particles in turbulent flows: monodisperse particles. *Phys. Rev. E* **97** (2), 023105.

Bragg, A.D., Ireland, P.J. & Collins, L.R. 2015 On the relationship between the non-local clustering mechanism and preferential concentration. *J. Fluid Mech.* **780**, 327–343.

Brandt, L. & Coletti, F. 2022 Particle-laden turbulence: progress and perspectives. *Annu. Rev. Fluid Mech.* **54**, 159–189.

CHEN, L., GOTO, S. & VASSILICOS, J. 2006 Turbulent clustering of stagnation points and inertial particles. *J. Fluid Mech.* **553**, 143–154.

CHUN, J., KOCH, D.L., RANI, S.L., AHLUWALIA, A. & COLLINS, L.R. 2005 Clustering of aerosol particles in isotropic turbulence. *J. Fluid Mech.* **536**, 219–251.

COLEMAN, S. & VASSILICOS, J. 2009 A unified sweep-stick mechanism to explain particle clustering in two- and three-dimensional homogeneous, isotropic turbulence. *Phys. Fluids* **21**, 113301.

DEJOAN, A. & MONCHAUX, R. 2013 Preferential concentration and settling of heavy particles in homogeneous turbulence. *Phys. Fluids* **25** (1), 013301.

ELPERIN, T., KLEEORIN, N. & ROGACHEVSKII, I. 1996 Self-excitation of fluctuations of inertial particle concentration in turbulent fluid flow. *Phys. Rev. Lett.* **77** (27), 5373–5376.

ESMAILY-MOGHADAM, M. & MANI, A. 2016 Analysis of the clustering of inertial particles in turbulent flows. *Phys. Rev. Fluids* **1** (8), 084202.

FABRI, A. & PION, S. 2009 CGAL: the computational geometry algorithms library. In *Proceedings of the 17th ACM SIGSPATIAL International Conference on Advances in Geographic Information Systems*, pp. 538–539. Association for Computing Machinery.

FARGE, M., PELLEGRINO, G. & SCHNEIDER, K. 2001 Coherent vortex extraction in 3D turbulent flows using orthogonal wavelets. *Phys. Rev. Lett.* **87** (5), 054501.

GOTO, S. & VASSILICOS, J.C. 2006 Self-similar clustering of inertial particles and zero-acceleration points in fully developed two-dimensional turbulence. *Phys. Fluids* **18** (11), 115103.

GOTO, S. & VASSILICOS, J.C. 2008 Sweep-stick mechanism of heavy particle clustering in fluid turbulence. *Phys. Rev. Lett.* **100** (5), 054503.

GUSTAVSSON, K. & MEHLIG, B. 2011 Ergodic and non-ergodic clustering of inertial particles. *Europhys. Lett.* **96** (6), 60012.

GUSTAVSSON, K., VAJEDI, S. & MEHLIG, B. 2014 Clustering of particles falling in a turbulent flow. *Phys. Rev. Lett.* **112** (21), 214501.

HIRT, C.W. & COOK, J.L. 1972 Calculating three-dimensional flows around structures and over rough terrain. *J. Comput. Phys.* **10** (2), 324–340.

IRELAND, P.J., BRAGG, A.D. & COLLINS, L.R. 2016*a* The effect of Reynolds number on inertial particle dynamics in isotropic turbulence. Part 1. Simulations without gravitational effects. *J. Fluid Mech.* **796**, 617–658.

IRELAND, P.J., BRAGG, A.D. & COLLINS, L.R. 2016*b* The effect of Reynolds number on inertial particle dynamics in isotropic turbulence. Part 2. Simulations with gravitational effects. *J. Fluid Mech.* **796**, 659–711.

KASBAOUI, M.H., KOCH, D.L. & DESJARDINS, O. 2019 Clustering in Euler—Euler and Euler—Lagrange simulations of unbounded homogeneous particle-laden shear. *J. Fluid Mech.* **859**, 174–203.

KOBBELT, L., CAMPAGNA, S., VORSATZ, J. & SEIDEL, H.-P. 1998 Interactive multi-resolution modeling on arbitrary meshes. In *Proceedings of the 25th Annual Conference on Computer Graphics and Interactive Techniques*, pp. 105–114. Association for Computing Machinery.

KUERTEN, J.G.M. 2016 Point-particle DNS and LES of particle-laden turbulent flow-a state-of-the-art review. *Flow Turbul. Combust.* **97**, 689–713.

LEVICH, E. 1987 Certain problems in the theory of developed hydrodynamical turbulence. *Phys. Rep.* **151** (3–4), 129–238.

MATSUDA, K., MAUREL-OUJIA, T. & SCHNEIDER, K. 2026 Multiresolution analysis on tessellation graphs for inertial particle dynamics. arXiv: 2605.19244.

MATSUDA, K., ONISHI, R., HIRAHARA, M., KUROSE, R., TAKAHASHI, K. & KOMORI, S. 2014 Influence of microscale turbulent droplet clustering on radar cloud observations. *J. Atmos. Sci.* **71** (10), 3569–3582.

MATSUDA, K., ONISHI, R. & TAKAHASHI, K. 2017 Influence of gravitational settling on turbulent droplet clustering and radar reflectivity factor. *Flow Turbul. Combust.* **98**, 327–340.

MATSUDA, K., SCHNEIDER, K., OUJIA, T., WEST, J., JAIN, S. & MAEDA, K. 2022 Multiresolution analysis of inertial particle tessellations for clustering dynamics. In *Proceedings of the Summer Program*. Center for Turbulence Research, Stanford University.

MATSUDA, K., SCHNEIDER, K. & YOSHIMATSU, K. 2021 Scale-dependent statistics of inertial particle distribution in high Reynolds number turbulence. *Phys. Rev. Fluids* **6** (6), 064304.

MAUREL–OUJIA, T., MATSUDA, K. & SCHNEIDER, K. 2024 Computing differential operators of the particle velocity in moving particle clouds using tessellations. *J. Comput. Phys.* **498**, 112658.

MAXEY, M. 1987 The gravitational settling of aerosol particles in homogeneous turbulence and random flow fields. *J. Fluid Mech.* **174**, 441–465.

MEIBOHM, J., GUSTAVSSON, K., BEC, J. & MEHLIG, B. 2020 Fractal catastrophes. *New J. Phys.* **22** (1), 013033.

MONCHAUX, R., BOURGOIN, M. & CARTELLIER, A. 2010 Preferential concentration of heavy particles: a Voronoï analysis. *Phys. Fluids* **22** (10), 103304.
MONCHAUX, R., BOURGOIN, M. & CARTELLIER, A. 2012 Analyzing preferential concentration and clustering of inertial particles in turbulence. *Intl J. Multiphase Flow* **40**, 1–18.
OKA, S. & GOTO, S. 2021 Generalized sweep-stick mechanism of inertial-particle clustering in turbulence. *Phys. Rev. Fluids* **6** (4), 044605.
ONISHI, R., BABA, Y. & TAKAHASHI, K. 2011 Large-scale forcing with less communication in finite-difference simulations of stationary isotropic turbulence. *J. Comput. Phys.* **230** (10), 4088–4099.
OUJIA, T., MATSUDA, K. & SCHNEIDER, K. 2020 Divergence and convergence of inertial particles in high-Reynolds-number turbulence. *J. Fluid Mech.* **905**, A14.
PINSKY, M., KHAIN, A. & KRUGLIAK, H. 2008 Collisions of cloud droplets in a turbulent flow. Part V: application of detailed tables of turbulent collision rate enhancement to simulation of droplet spectra evolution. *J. Atmos. Sci.* **65** (2), 357–374.
ROBINSON, A. 1956 On the motion of small particles in a potential field of flow. *Commun. Pure Appl. Maths* **9** (1), 69–84.
SAITO, I. & GOTOH, T. 2018 Turbulence and cloud droplets in cumulus clouds. *New J. Phys.* **20** (2), 023001.
SAVITZKY, A. & GOLAY, M.J.E. 1964 Smoothing and differentiation of data by simplified least squares procedures. *Anal. Chem.* **36** (8), 1627–1639.
SCHWARTZ, L. 1950 *Théorie Des Distributions*, vol. 2. Hermann. (1re éd. 1950–1951); nouvelle éd. 1966.
SIMONIN, O., ZAICHIK, L.I., ALIPCHENKOV, V.M. & FÉVRIER, P. 2006 Connection between two statistical approaches for the modelling of particle velocity and concentration distributions in turbulent flow: the mesoscopic Eulerian formalism and the two-point probability density function method. *Phys. Fluids* **18** (12), 125107.
SQUIRES, K.D. & EATON, J.K. 1990 Particle response and turbulence modification in isotropic turbulence. *Phys. Fluids A: Fluid Dyn.* **2** (7), 1191–1203.
SQUIRES, K.D. & EATON, J.K. 1991 Preferential concentration of particles by turbulence. *Phys. Fluids A: Fluid Dyn.* **3** (5), 1169–1178.
TSINOBER, A. & LEVICH, E. 1983 On the helical nature of three-dimensional coherent structures in turbulent flows. *Phys. Lett. A* **99** (6–7), 321–324.
VORONOI, G. 1908 Nouvelles applications des paramètres continus à la théorie des formes quadratiques. Deuxième mémoire. Recherches sur les parallélloèdres primitifs. *J. Reine Angew. Math.* **134**, 198–287.
WILKINSON, M. & MEHLIG, B. 2005 Caustics in turbulent aerosols. *Europhys. Lett.* **71** (2), 186.
WILKINSON, M., MEHLIG, B. & BEZUGLYY, V. 2006 Caustic activation of rain showers. *Phys. Rev. Lett.* **97** (4), 048501.
WOITTIEZ, E.J.P., JONKER, H.J.J. & PORTELA, L. 2009 On the combined effects of turbulence and gravity on droplet collisions in clouds: a numerical study. *J. Atmos. Sci.* **66** (7), 1926–1943.